Graciano Bay de Souza

Coating of carbon support fibers with titania by Atomic Layer Deposition

Florianópolis, SC-Brasil

13 de janeiro de 2023

Graciano Bay de Souza

Coating of carbon support fibers with titania by Atomic Layer Deposition

Tese submetida ao Programa de Pós-Graduação em Ciências e Engenharia de Materiais para a obtenção do título de doutor em Ciência e Engenharia de Materiais.
Orientadores: Prof. Carlos Renato Rambo, Dr. (UFSC) e Prof. Rolf Janßen, Dr. (Hamburg University of Technology)
Coorientadores: Prof. Dachamir Hotza, Dr. e Profª. Kaline P. Furlan Dr. Sc. Eng.

Florianópolis, SC-Brasil
13 de janeiro de 2023

Ficha de identificação da obra elaborada pelo autor,
através do sistema LATEX.

Graciano Bay de Souza

Coating of carbon support fibers with titania by Atomic Layer Deposition

O presente trabalho em nível de doutorado foi avaliado e aprovado por banca examinadora composta pelos seguintes membros:

Prof. Lucas Berti Dr.
Universidade Federal do Parana

Prof. Luiz Fernando Belchior Dr.
Universidade Federal de Santa Catarina

Prof. Sergio Goméz Gonzáles Dr.
Universidade Federal de Santa Catarina

Certificamos que esta é a **versão original e final** do trabalho de conclusão que foi julgado adequado para obtenção do título de doutor em Ciência e Engenharia de Materiais.

———————————————
Prof. Dr. João Batista Rodrigues Neto
Coordenador do Programa

———————————————
Prof. Carlos Renato Rambo, Dr.
Orientador

Florianópolis, SC-Brasil, 13 de janeiro de 2023.

Este trabalho é dedicado à toda comunidade acadêmica.

ACKNOWLEDGEMENTS

relevant topics on the thesis subject, for supporting me when dealing with the bacterial nanocellulose, and always encouraging me.

I am indebted to the ceaseless support of my cherished friend MEng. Katherina Lewandowski for been an always accessible shoulder and attainable to help me out with all sort of issues, from the most ordinary of the daily academic tasks and general surviving in Hamburg, to the more complex one-time painstaking *Anmeldebescheinigung*. Without Bärbel Rademacher Secretariat of the Institute Advanced Ceramics at Hamburg University of Technology expert help and encouragement, I would not have found such decent apartment to live in Harburg in such short time. Which was the first basic need in Hamburg for conducting my research. All the other members of the of the Institute Advanced Ceramics at TUHH whom I could not list here, due to necessary text length constrains, for the general support into how to use the facilities and where to find the tools for my experiments.

I extend my thanks to my colleagues: MSc Mirele Teixeira, for giving me the opportunity to guide and introduce to the marvels of the German bureaucracy, for discussing various research issues at a high level; Rafael Vidal for giving me clues on-time to what to do first in TUHH; Marcelo Barros for keeping the doors open and inspiring me to go forward as well as essential housing and pricing advice for Hamburg; Camila Daniela Moura Nickel for, despite the short time, been an excellent company, sharing the misadventures of the life abroad and discussing important research topics; Georges Pães de Barros for assisting me, from day one until the end, with a wide variety of technicalities, for stimulating my research and teaching me some key electronic concepts.

To Alexis Huf and Dr. Gustavo Zambonin from UFSC for adapting, fixing, maintaining and helping me with blessed updated LaTeXclass for UFSC's standards. To the developers and the entire community of the TeXand LaTeX, especially to the folks at StackExchange TeX.

I am also very grateful for my, only and unrepeatable, family support and encouragement.

Parts of this thesis were adapted, with permission, from Graciano B. De Souza et al. in Advances in Materials Science and Engineering ⓒ ⓘ Hindawi (1).

RESUMO ESTENDIDO

Introdução

O design da natureza apresenta grande eficiência, suas estruturas são resultados de milênios de seleção natural. Replicar essas estruturas pode nos auxiliar na busca de eficiência, por isso o uso de materiais biomórficos se torna tão relevante.

Algumas bactérias produzem fibras de celulose para se proteger de agressões do meio ambiente. Estas fibras são nanométricas e formam uma estrutura de interesse, pois são uma forma eficiente que a bactéria desenvolveu para se defender mecânica e quimicamente. Essa estrutura biomórfica apresenta algumas características: alta área superficial, boa permeabilidade e alta pureza. A geometria do corpo poroso de fibras pode ser controlada com o uso de diferentes recipientes, agitação, e meio de cultivo da bactéria. A pirólise destas fibras nos permite obter uma estrutura de carbono.

Outros materiais com estrutura similar podem ser produzidos, por exemplo, através da eletrofiação de polímeros e posterior pirólise das fibras. Feltros de carbono de alta pureza são amplamente conhecidos e estão disponíveis comercialmente.

Estes substratos de carbono podem ser recobertas com outros materiais, tais como óxidos metálicos. Para que tal recobrimento retenha o máximo possível da estrutura biomórfica original, as camadas deste material a ser depositado devem ter uma pequena espessura. Camadas de dimensão nanométrica podem ser conseguidas através da deposição atômica (Atomic Layer Deposition, ALD), uma técnica similar à deposição de vapor químico (CVD). Neste processo, as moléculas adsorvem à superfície em vez de reagir quimicamente.

Óxidos metálicos são freqüentemente combinados com carbono em eletrodos de capacitores. Um capacitor é um componente eletrônico passivo que armazena energia elétrica em um campo elétrico e pode fornecer essa energia na forma de uma corrente elétrica. Existem diferentes categorias de capacitores que armazenam energia através de diferentes fenômenos.

Objetivos

Neste trabalho o principal objetivo foi investigar a seguinte hipótese: se a deposição atômica em substratos de alta porosidade pode ser bem sucedida, ou seja sem regiões com excesso de deposição nem regiões com falta. Mais especificamente em materiais de estrutura fibrosa, com fibras de espessura de no máximo $2\,\mu m$. Os substratos selecionados foram a nanocelulose bacteriana (BNC) e o feltro de carbono Kynol.

Esse estudo e investigação compreendeu o entendimento dos princípios da deposição atômica, parâmetros de processamento, procedimentos práticos e operacionais. E para avaliar a efetividade deste processo o uso de técnicas de caracterizações, incluindo mas não se limitando a, microscopia eletrônica de varredura, difração de raios-X e adsorção de nitrogênio. Em uma etapa adicional algumas amostras foram queimadas para remoção total do substrato fibroso.

Como objetivo secundário foram avaliadas algumas propriedades elétricas dos substratos, após recobrimento. Devido à alta área superficial esperada para ambos substratos optouse por montar um eletrodo para capacitor. Isso incluiu a construção do eletrôdo em si, a montagem da célula de medida, aquisição dos dados e a espinhosa interpretação destes resultados.

Materiais e Métodos

Os materiais utilizados foram a nanocelulose produzida pela bactéria Gluconacetobacter Xylinus e o tecido-não-tecido feltro de carbono ACN-211-20 da Kynol. A celulose foi, após esterilização, submetida a sucessivas trocas de solvente, de água para etanol, de modo a permitir a secagem super-critica. Na secagem super-crítica o etanol é gradualmente substituído por CO_2 líquido e em seguida aquecido sob pressão. Este processo permite a remoção da fase líquida sem perda da nano estrutura, e se obtêm assim um aerogel de nanocelulose bacteriana. As amostras de Kynol não foram submetidas a outros tratamentos. Ambas amostras foram cortadas com as dimensões aproximadas de $5\,mm \times 10\,mm$ e então posicionadas no centro do reator de deposição atômica. O precursor utilizado na deposição foi o isopropóxido de titânio e como reagente a água deionizada. Ambas as amostras foram submetidas, separadamente, ao processo de deposição compreendendo 700 ciclos. Os tempos de pulso/exposição/purga do isopropóxido de titânio e da água foram de 1/30/60 e 0,1/30/90 segundos, respectivamente.

Após a deposição, o aerogel de nanocelulose bacteriana foi submetido a pirólise, sob atmosfera inerte de N_2, com uma taxa de aquecimento de $10\,°C\,min^{-1}$ até atingir o platô de $800\,°C$, e este foi mantido por duas horas. Uma amostra de Kynol foi queimada em um forno mufla a uma taxa de aquecimento de $10\,°C\,min^{-1}$ e temperatura de patamar de $400\,°C$, mantida por duas horas.

As amostras foram caracterizadas utilizando diversas técnicas, incluindo, mas não se limitando a, microscopia eletrônica de varredura, difração de raios-X, espectroscopia Raman e área superficial por adsorção de nitrogênio.

Para caracterização eletrônica foram produzidos eletrodos. As amostras foram maceradas e dispersas com um ligante polimérico em um solvente orgânico, numa proporção de `10:1:1000` (carbono, PVDF, metilpirrolidona), em seguida essa pasta foi espalhada, em uma área de aproximadamente $0.5\,cm \times 0.5\,cm$ sobre uma placa de alumínio formando assim um eletrodo.

Os eletrodos foram então avaliados através da voltâmetria cíclica ($5\,mV\,s^{-1}$ a $100\,mV\,s^{-1}$) e impedância ($100\,kHz$ e $0.001\,kHz$), em um aparato com dois eletrodos (amostra e referência de Pt) em uma solução aquosa de 1 mol de KOH.

Resultados e Discussão

Nas imagens obtidas através da microscopia eletrônica de varredura é possível observar que a estrutura morfológica das fibras de ambas amostras se mantém praticamente inalteradas após a deposição atômica, isso indica que o processo de deposição ocorreu de maneira satisfatória. A amostra de aerogel de nanocelulose bacteriana pirolisada apresentou uma distorção das fibras e encolhimento, embora tenha mantido a estrutura. A amostra de Kynol submetida a queima apresentou longas fibras ocas, presume-se de TiO_2 uma vez que não foi efetuada uma análise específica desta amostra, sem grandes mudanças na estrutura morfológica.

Na difração de raios-X foi possível identificar os picos de cristalinidade referentes a celulose e ao carbono nas amostras puras (antes da deposição). Após a deposição foram identificados também os picos da fase Anátase do TiO_2. Não era esperada a estabilidade desta fase após o tratamento térmico uma vez que foi ultrapassada a temperatura de transição de fase, porém através de posterior pesquisa bibliográfica se constatou que tal fenômeno é conhecido no processamento de nano partículas e filmes finos de TiO_2. O espectro Raman revelou dois picos das bandas D e G do carbono, deslocados nas amostras de Kynol antes da deposição. A proporção entre os picos, 0.917, que correlaciona à desorganização das

diferentes formas de carbono, encontrada, está de acordo com resultados de outros autores para materiais similares.

Como esperado, a área de superfície específica diminuiu com a deposição de titânia já que as fibras aumentam em diâmetro e por consequência a distancia entre elas, o poro, diminui. Resultados similares foram observados para nanopartículas de óxido de ferro revestidas através de ALD. Embora a diminuição seja pequena para a amostra de Kynol, de $1\,695\,\mathrm{m^2\,g^{-1}}$ para $1\,480\,\mathrm{m^2\,g^{-1}}$, foi considerável para a amostra de nanocelulose, de $200\,\mathrm{m^2\,g^{-1}}$ para $50\,\mathrm{m^2\,g^{-1}}$. Esta pequena área indica um comportamento potencialmente não otimizado durante alguma etapa do processamento, de modo que, existe a forte possibilidade de ao invés do revestir individualmente as fibras, estas tenham se aglomerado e sido revestidas como uma única peça. A área relativamente menor da nanocelulose bacteriana também poderia ser atribuída à deformação estrutural da amostra, antes mesmo da deposição, durante o manuseio e corte. O aumento de área para a nanocelulose pirolisada, $175\,\mathrm{m^2\,g^{-1}}$, está associado à provável ruptura da fibra e/ou delaminação do revestimento, e alguma perda de estrutura.

Na voltâmetria cíclica a amostra de nanocelulose bacteriana apresentou uma curva mais próxima a de um pseudocapacitor, curva semelhante a uma bandeira, enquanto a amostra de Kynol teve uma curva com esse comportamento menos pronunciado.

No gráfico Nyquist é possível observar que a amostra de nanocelulose bacteriana diminuiu tanto a impedância real quanto a impedância imaginária. Esta mudança pode ser atribuída à dificuldade de difusão sob freqüências mais baixas, que se torna menos importante à medida que a freqüência aumenta. No gráfico Bode todas as amostras exibiram uma resposta do tipo *capacitor-quase-ideal*.

Na carga-descarga galvanostática a amostra Kynol exibe um perfil quase triangular de um armazenamento de carga do tipo supercapacitiva. A amostra de nanocelulose bacteriana pirolisada exibiu um comportamento de armazenamento de carga semelhante ao de uma bateria. A capacitância específica, a $5\,\mathrm{mV\,s^{-1}}$, sugere uma correlação com a área superficial. No entanto, esta relação não mantém verdadeira à medida que se aumenta a taxa de varredura.

Considerações Finais

Foi demonstrado que a nanocelulose bacteriana biomórfica e os tecidos-não-tecidos de carbono podem ser recobertos com sucesso e conformidade pelo processo de *Atomic Layer Deposition*, mantendo sua área superficial na mesma ordem de grandeza. Devido a sua pequena espessura a camada de TiO_2 permitiu que a fase Anatase se mantivesse estável mesmo após o tratamento térmico. A camada de deposição também mantém sua forma e estrutura quando a fibra é removida por queima, gerando fibras ocas de titânia com espessura de parede nanométrica. A despeito da baixa capacitância, as outras propriedades podem permitir que as fibras de carbono revestidas com titânia sejam usadas em dispositivos eletroquímicos de armazenamento de energia. Uma vez que alguns parâmetros sejam ajustados, tais como, a espessura de deposição, temperatura de pirólise, composição e concentração de eletrólitos e a proporção de massa do material ativo no conjunto do eletrodo, resultados mais favoráveis podem ser encontrados em trabalhos futuros.

Palavras-chave: Deposição atômica. Nanocelulose bacteriana. Kynol. TiO_2. Aerogel.

ABSTRACT

Carbon fibers are materials with a very high surface, interesting for applications such as filters, fire-resistant heat insulation, photocatalysis, and capacitor electrodes. In this work, two different substrates, carbon felt and bacterial nanocellulose (BNC), were coated by TiO_2 with atomic layer deposition (ALD). After deposition, the templates were pyrolyzed . The microstructure evolution of the 3D interlocked-fibers structures was characterized by scanning electron microscopy and nitrogen adsorption surface area after each step. Stable anatase was present as a single TiO_2 phase even after heat treatment at 800 °C. Moreover, electrochemical impedance spectroscopy and constant current charge-discharge were employed to investigate the electrochemical properties of the samples. Our results show that all samples display a uniform layer after ALD and that the surface area decreased with increasing number of ALD cycles. After burnout, the 3D structures presented a straw-like appearance for the shells. Nonetheless, both samples presented a power density comparable to a porous NiO/C, with the pyrolyzed bacterial nanocellulose sample displaying a higher pseudocapacitance performance than the carbon felt samples.

Keywords: Atomic Layer Deposition. Bacterial Nanocelullose. Kynol. TiO_2. Aerogel.

LIST OF TABLES

LIST OF FIGURES

LIST OF ABBREVIATIONS

ALD   Atomic Layer Deposition

ALE   Atomic Layer Epitaxy

BNC   Bacterial Nanocelullose

C_p Specific Capacitance

CVD   Chemical Vapor Deposition

CV   Cyclic Voltammetry

NMP   N-Methyl-2-pyrrolidone

PVDF   Polyvinylidene DiFluoride

S_{BET} Surface area via Brunauer Emmett Teller

SEM   Scanning electron micrography

SSA   Specific Surface Area

TMA   Trimethylaluminum

TIPP   Titanium isopropoxide

WP   Weight Proportion

CONTENTS

1 Introduction

"Knowledge is certainly one of the means of pleasure, as is confessed by the natural desire which every mind feels of increasing its ideas. Ignorance is mere privation, by which nothing can be produced; it is a vacuity in which the soul sits motionless and torpid for want of attraction, and, without knowing why, we always rejoice when we learn, and grieve when we forget."

Samuel Johnson, 1759, Rasselas, Prince of Abyssinia, Chapter 11.

Nature's design is highly efficient; they are a product of centuries of natural selection. Replicating these structures can help us reach efficiency; that is why biomorphic materials attract such attention. In addition to these qualities, the biomorphic replica also brings the possibility of being a carbon source for the formation of carbon-based compounds and composites (2).

Some bacteria can synthesize high purity cellulose fibers as shielding from the environment. These fibers are nanometric and compose the structure of interest to us; they are what the bacteria uses to protect itself chemically and mechanically while retaining its necessary water. The geometry of this porous body can be easily tweaked into many bulk forms just by changing the culture medium container shape, and its fiber density can be tailored according to growth parameters (3).

The use of natural structures presents a benefit, having a design and engineering of relentless evolution. The bacterium organizes its fibers in a apparently disordered way, but the size, length, and grouping of the fibers happen very efficiently because its survival depends on it. Although the bacteria produce the cellulose fiber in a aqueous environment this limitation can be circumvented by supercritical drying, thus generating a Bacterial Nanocelullose (BNC) aerogel.

These fibers are arranged so that they possess a high specific surface area and have been of much interest as gas-sensors, and capacitor electrodes components. The polymeric nature of the cellulose would not be suitable for all of these applications. By pyrolyzing these cellulose fibers, one can obtain a structure that will be both a carbon source and a biomorphic template.

Another similar material, with a much larger fiber diameter, are carbon fiber non-oven textiles, which are a felt-like material obtained from pyrolysis of synthetic polymer fiber. These carbon felt are commercially available and are easily accessible.

Such carbon templates can be coated with other materials of interest, such as metal oxides. Most processes, like dip-coating, do not retain the original biomorphic nanostructures. This happens because the slurry layer is too thick, thus thin layers are desirable. Other process, like evaporation deposition have a limited control over the thickness (4, p.13, 5) and limited range of material selection (6, p.26). Sputtering on the other hand may not be suited for coating pores deeper than $200\,\mu m$ (7). Nanometric size layers can be achieved through Atomic Layer Deposition (ALD), a technique similar to Chemical Vapor Deposition (CVD) as it will be explained in Section 3.1 (page 30) . Figure 1 illustrates a simplified ALD cycle.

ALD however, has been usually applied to planar surfaces, such as 2D semiconductors, or in some cases nanowires but rarely on μm (bulk) sized porous sample. This is the main purpose of this work, to test if the BNC can be coated via ALD and still maintaining its biomorphic nanostructure while serving as a carbon source.

Metal oxides combined with carbon are often used as capacitors electrode (9, p.71). A capacitor is a passive electronic component that stores electrical energy in an electric field

Figure 1 – ALD Cycle scheme
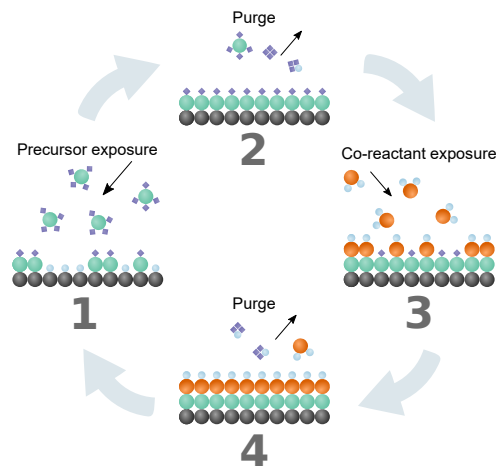
Sorce: Author, inspired by (8).

and can deliver this energy in the form of an electrical current. There are different types of capacitors that store energy through different physical phenomena. Thus titanium oxide was chosen as deposition layer.

By providing more evidence of the ALD applied on bulk porous materials we would be expanding the limits of the technique. The high surface area of BNC means that, if successful, it could be an excellent active material for a capacitor, since the capacitance is directly correlated to surface area.

Some portions of this thesis were adapted, with permission, from Graciano B. De Souza et al. in Advances in Materials Science and Engineering ⓒⓘ Hindawi (1).

2 Objectives

> "If we wait for the moment when everything, absolutely everything is ready, we shall never begin"
>
> Ivan Turgenev.

In this work, the main objective was to test if a bulk highly porous materials, more specifically fibrous materials with fibers below 2 μm thick, could be coated via ALD in a conformal way and become a carbon source. Such materials were the bacterial nanocellulose aerogel, and the carbon felt Kynol. In order for the BNC to become a carbon source it was also tested if the structure would be kept after a pyrolysis process. An additional process performed on the Kynol sample was the burnout, to inspect the remaining structure after removing the fibers.

A secondary objective was to examine the electrical proprieties of these samples as a possible application for a capacitor, due to its morphological and chemical characteristics. For example titanium oxide has a dielectric constant of 40 to 170 (10, 11) and energy bandgap of 2.9 eV to 4.7 eV (12, 13, 14). So this included the assembly of an electrode, measuring cell, data acquisition, and the puzzling interpretation of the results. On Table 1 a brief overview of the experimental planning is displayed.

Table 1 – Experimental procedure summary

| Sample | Processes | | | |
	Pre	ALD cycles	Post	Additional
BNC	Sup. drying	700	Pyrolysis	-
Kynol	-	700	-	Burnout

Source: Author.

This investigation encompassed the comprehension of the deposition principles, processing parameters, and practical and operational procedures. Make use of a variety of characterization techniques available, including, but not limited to, electron scanning microscopy, X-ray diffraction and nitrogen adsorption.

3 Theoretical Framework

███████████████████████████████████

> " Alas! In this prison must I stick?
> This hollow darkened hole of brick,
> Where even the lovely heavenly light
> Shines through stained glass, dull not bright.
> Hemmed in, by heaps of books,
> Piled to the highest vault, and higher,
> Worm eaten, decked with dust,
> Surrounded by smoke-blackened paper,
> Glass vials, boxes round me, hurled,
> Stuffed with Instruments thrown together,
> Packed with ancestral lumber –
> This is my world! And what a world! "
>
> Johann Wolfgang von Goethe, Faust Part I,
> 400th verse.

3.1 ATOMIC LAYER DEPOSITION

The Atomic Layer Deposition process descends from Chemical Vapor Deposition; it exposes a surface, separately, to at least two different gaseous *molecules*, the precursor and the co-reactant. When this exposure is done with the proper parameters, the reaction between the surface and each gas will form a thin layer. Because the gaseous molecules can only adsorb to available sites the reaction is called self-terminated. The individual steps, like pumping and purging each of the gases, that are necessary to form a single layer compromise what is known as a cycle (8).

Maybe because of its chemical parentage, most of the first few publications on the subject were in chemistry journals. These first studies were published, around 1950 and 60-decade, in the former Soviet Union, notably by Aleskovskii and S. I. Kol'tsov, under the name of Molecular Layering (15, 16). Unaware of those findings, the physicists from Finland, Tuomo et al., were researching what they first called Atomic Layer Epitaxy (ALE) in a famous patent (17). As the interest at the time was on crystalline films the name was reasonable, however the original intention was to referrer epitaxyal as to the ordered layering formed by the sequential gas exposure, rather then the crystalline structure (18, p.104). Around 2000, the broader term *Atomic Layer Deposition* was adopted and ended the confusion between crystalline and amorphous films (8, 16), this change can be observed in the word relative frequencies, in English, books plot (19).

Figure 2 – Frequency of ALD and ALE terms in published books

(a) Frequency from 1940 to 2019

(b) Frequency cropped from 1993 to 2011
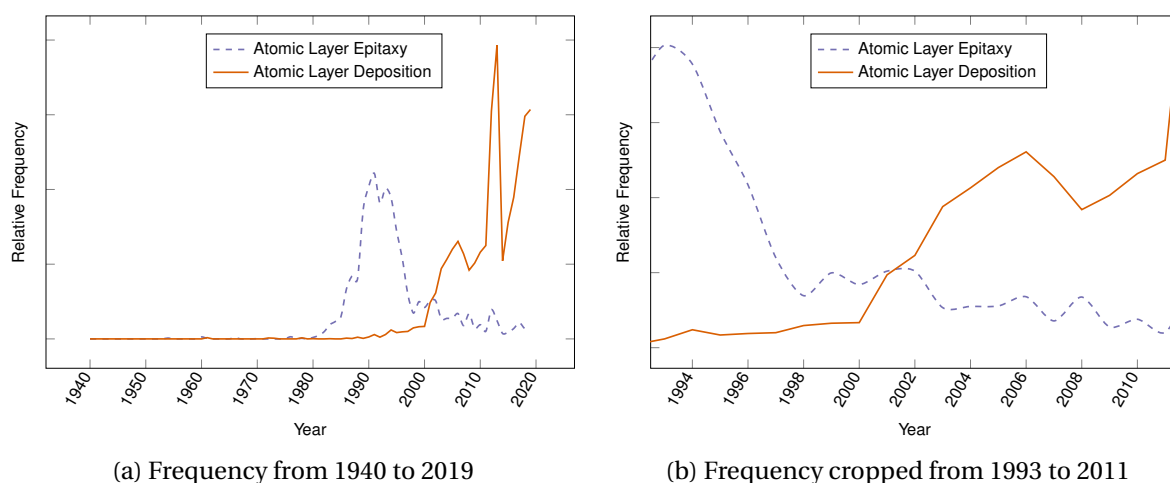
In (a) the relative frequency for ALD and ALE terms since 1940 until 2019. In (b) the data is cropped to display the decline of ALE in favor of ALD between 1993 and 2012.
The relative frequency is referenced to the most common words/expressions in English, during each time span, and not in relation to each term.
Source: Author, retrieved from (19).

The Russians, who got the name more technically precise at first, started by depositing chlorides paired with water vapor, such as $TiCl_4$ / H_2O and $GeCl_4$ / H_2O, to generate

thin films of titania and germania respectively. While the Finnish group focused on zinc sulfide, tin (IV) oxide, and gallium phosphide (16).

The ALD name suggests that an atom-thick layer is deposited on a substrate at a time. The so-called **atomic** layer deposition label is partially correct. The adsorption itself may consist of a molecule, such as $TiCl_4$ or H_2O, for example, thicker than an atom but still very close in scale. So, the layer formed maybe indeed restrained to a few atoms (20). Figure 1 illustrates a simplified ALD cycle.

Figure 4 – Layer deposition using Titanium isopropoxide and water.
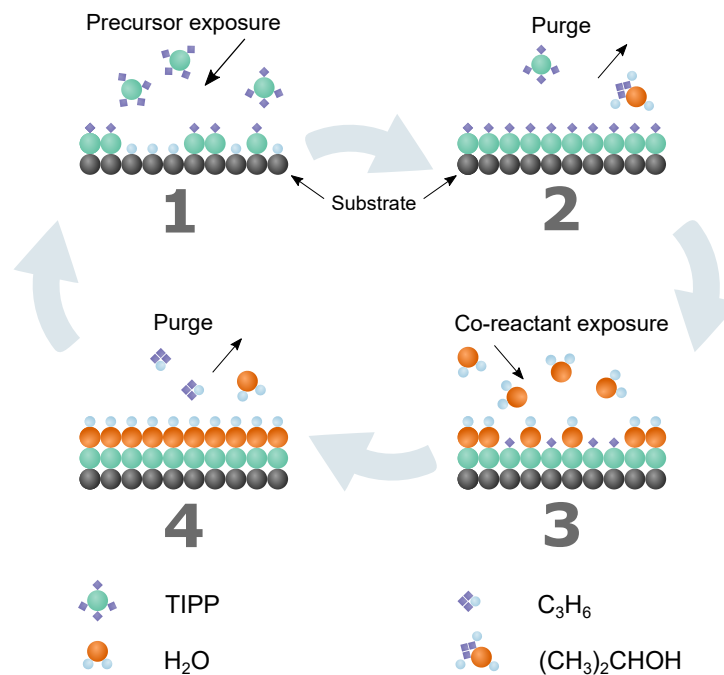
Source: Author, inspired by (21).

These reactions happen inside a enclosed compartment, a *reactor*, where the gases' flow, heat, and pressure are carefully controlled. ALD reactors are usually one of two types: Temporal or Spatial (22). When substrate remains in a fixed location and the precursor and co-reactant gases flow over time, it's classified as a temporal reactor. The substrate is placed inside the reactor chamber, and the precursor and co-reactant are injected. Different nozzles or a single inlet may be used for the reactants, depending on whether a carrier gas is used or not. The purge is usually performed through a single outlet. This design allows for batch manufacturing, but the pressure restrictions imply a limitation on the chamber volume (23, 20). Figure 5 displays an ALD temporal design.

Because the whole chamber is exposed to the complete cycle of reactant and co-reactant exposure, deposition may occur inside the walls and other reactor parts. This chamber buildup and precursor waste, however, can be overcome if different parts of the reactor get exposed to only one species during the whole cycle: a space-based design (22).

On the spatial design the different gas zones are fixed, and the substrate moves inside the reactor continuously, as shown in Figure 6. The purge time does not exist in

Figure 5 – Simplified ALD temporal design with essential components
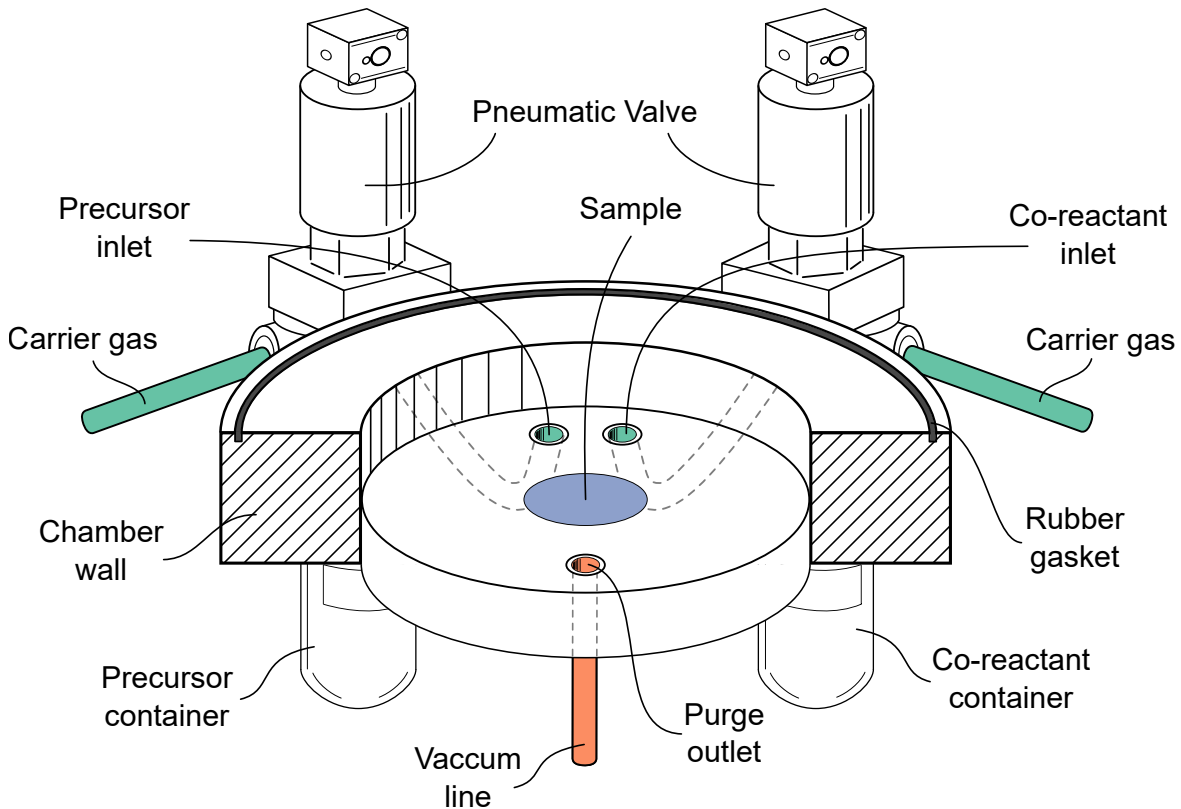
Source: Author, inspired by (24).

these spatial designs because the different zones are separated by an inert gas curtain, or gas-bearing, thus allowing for faster processing. These reactors may also vary in shape and size, depending on substrate dimensions (22).

Figure 6 – Simplified ALD spatial process sketch
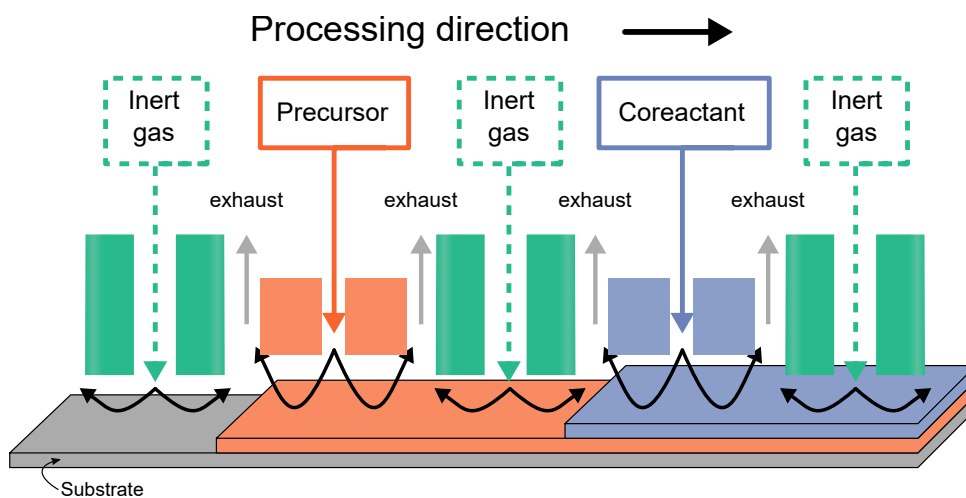
Source: Author, inspired by (25, p.14).

The reason why ALD can form such thin layers is that the process relies on a self-limiting reaction. The number of adsorption sites for a given molecule is limited. Once the

surface has been covered evenly, no more long-lasting adsorption occurs at the given temperature and pressure, regardless of the exposure time. In a binary cycle, as demonstrated in Figure 4, a gaseous spice is pumped into a chamber containing the substrate; this is the first step in the cycle, usually called Precursor Pulse or **Exposure**. The next step is the purge, where all the remaining and unreacted molecules get pumped out. In the third step, the substrate is exposed to the co-reactant, the second molecule will yield a surface chemically attractive to the adsorption of another layer of the precursor. The last step is again a purge of the co-reactant (8, 20).

Once a precursor molecule meets the surface, it may or may not adsorb; this is the concept of sticky probability. The *sticky probability* equation can be expressed from the Langmuir's adsorption isotherm (26):

$$S = S_0(1-\theta) \tag{1}$$

where S_0 is the initial sticking probability, and θ is the fraction of the covered surface.

In reality, the mechanism can be intricate because some molecules will chemisorb directly, while others will first physisorb and later turn into chemisorption. As the available sites for adsorption get occupied, the probability of course changes with time until it reaches zero in an ideal situation (27, p.5). The sticking coefficient is the ratio between the number of molecules that reach the surface and the number of molecules that adsorb. It is connected to a series of factors such as temperature and kinetic energy of the molecules (28).

ALD may have a very narrow processing window: at low temperatures and low sticking coefficient may imply that not enough energy is reached to adsorb; at low temperatures but higher sticking coefficient, molecules might condense, forming clumps instead of a thin layer; high temperature and low sticking coefficient will promote the desorption of the molecules from the surface; high temperature and high sticking coefficient can cause molecules to decompose (29).

While the halides have been very popular in the early stages of ALD, other compounds are now in focus; Organometallics, these compounds tend to have lower toxicity and be less prone to cause corrosion on the reactor. One example of halide is the binary $TiCl_4$ and Ammonia, which not only are extremely hazardous substance (30) but also generates hydrogen chloride gas as a byproduct (29). As an example of metalloorganic byproduct, the binary of Titanium isopropoxide (TIPP) and water generates isopropanol (propan-2-ol) (31).

The deposition can occur in many different substrates, shapes, and sizes, from planar to porous. The early researches from Shevjakov et al., in 1967, were done on silica, very porous substrate (16).

The atomic layer deposition on a flat planar surface is distinct from that in a highly mesoporous or microporous substrate; the gas flows differently. A common way to differentiate the gas flow is with the ratio between the mean free path (λ) of the molecule and a length (d), in this case, the pore diameter, this parameter (K_n) is known as Knudsen

Number:

$$K_n = \frac{\lambda}{d} \tag{2}$$

If the pore diameter is considerably smaller than the mean free path ($K_n \leq 0.01$), then the particle-surface phenomena become more prominent; this is known as Free Molecular Flow. Moreover, if the pore diameter is much *larger* than the mean free path ($K_n \geq 10$), then particle-particle interactions will dominate, this is known as Continuum Flow, or Viscous Flow (33).

By expanding the mean free path equation, we can see some of the main factors influencing thermal ALD:

$$\lambda = \frac{k_B T}{\sqrt{2}\pi d_m{}^2 P} \tag{3}$$

where k_B is the Boltzmann constant, T the temperature, d_m the diameter of the molecule, and P the pressure. Considering the same reactivity, or sticking coefficient, and a sufficient number of molecules to cover the surface, the remaining factors are Temperature, Pressure, and the Knudsen number (substrate dependent) (26). A summary of the factors, and their respective effects, is presented in Table 2. It is important to reassure that these factors are usually interdependent and highly related to precursor choice, sample material and reactor design, as can be seen in Figure 7.

Table 2 – ALD physiochemical factors and processing parameters effects

Factor	Low	Medium	High
Physiochemical			
Knudsen numb.	Molecular flow	Molecular flow	Continuum flow
Sticking coef.	Reversible adsorption	Adsorption	High eff. adsorption
Available mol.	Insufficient coverage	Surface saturation	Precursor waste [†]
Processing			
Temperature	Condensation	Adsorption	Desorption [*]
Pressure	Poor precursor carrier	Balanced	Lower interdiffusion
Exposure time	Insufficient coverage	Complete coverage	Longer cycle

[†] A CVD-like reaction may happen inside the reactor.
[*] Decomposition may also occur.
 Source: Author, adapted from (20, 27, p.6-8, 29, p.5-8, 34, p.2234, 35, 36, 37).

Deposition on a nanoporous or nanofibrous substrate may be significantly different because the flow regime can be distinct, but also the surface area may change as the layers stack (26). Pores will be covered internally and thus decrease in surface area, while fibers will be covered externally and increase the surface area up to a certain point; this is illustrated in Figure 8.

Figure 7 – ALD parameters relation

Precursor/sample related		Reactor related
Knudsen number		Exposure time
Sticking coefficient	⟷	Molecular concetration
Temperature		Pressure
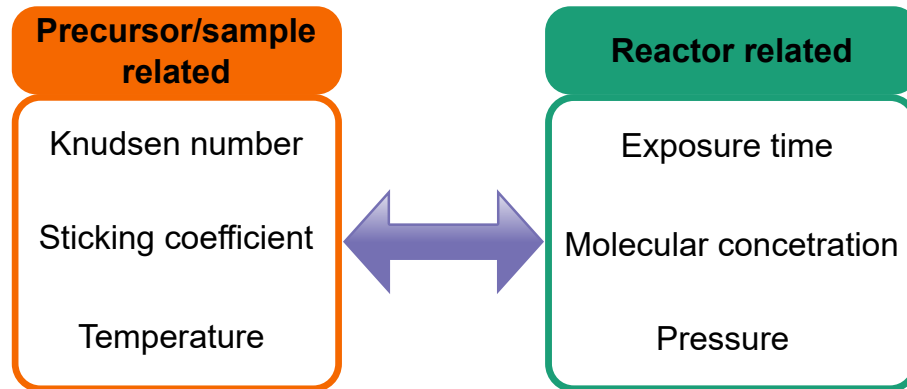
Source: Author, inspired by (35, 36, 37).

Elam et al. demonstrated, experimentally, that when performing ALD on a nanoporous filamented material, the increase in mass is quadratic, but the increase in radius is linear. In contrast to planar substrates where both would be linear (38). Quadratic mass growth can be theoretically derived from the geometric fact that the volume of a cylindrical filament or fiber increases with the difference in the squares of the radii.

On flat substrates, the thickness of the layers is usually analyzed with the optical spectroscopic ellipsometry technique (20). This method involves shooting polarized beam lights on the substrate at a certain angle, depending on the layer material. And then measuring the difference in polarization of the reflected beams. Different wavelengths of the light will change polarization more or less depending on the deposited thickness (39, p.64-66).

Figure 8 – ALD Layers in pores and fibers

Porous substrate

First cycle   Second cycle

Fiber substrate
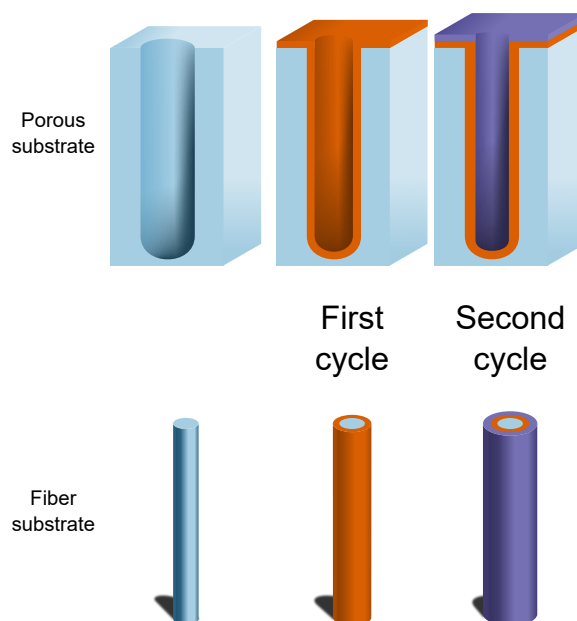
Source: Author, inspired by (26).

However, as the name implies, this technique requires the layers to be optically available for a direct beam, which is not always the case with a porous substrate.

When performing a deposition on new materials, such as porous samples for example, it is common to include a silicon as a control substrate in the reactor chamber. And then analyze the deposition onto this plane silicon substrate instead of the actual sample. This indirect measurement allows for a straightforward comparison between samples in a different run, for example, but does not measure the actual thickness of the layers on the sample substrate itself.

Another alternative to measuring the thickness of the deposited layers on porous substrates is a modification of the ellipsometry, sometimes called *ellipsometric porosimetry*. In this technique, an known adsorptive material gradually fill the pores and thus allow changes in the polarization to be measured (40).

3.1.1 ALD State of the Art

The capacity of ALD to form a controlled thin film, even on very porous and intricate structures, had been already been demonstrated before. For example, Furlan et al. demonstrated that α-Al_2O_3 ALD can be applied to micro-sized polymer particles to create a highly porous inverse opal structure with large domains of identical crystalline orientation. These structures provide higher thermal stability and may be used in filters (41).

There are several studies on ALD deposition temperature, as it is a key processing factor and varies by a lot depending on the precursor composition. Zhu et al. investigated the effects of deposition temperature on SnO_2 ALD and the effect of film thickness on the crystallographic state. They have found that below 165 °C the process tends to favor chemical reactions rather than surface adsorption, generating a CVD process where the thickness is not finely controlled as in ALD. At higher temperatures, they were able to deposit thin (> 40 nm) films of SnO_2 on carbon nanotubes and test them as anodes, finding a high specific capacitance (42). This is in contrast to titanium isopropoxide which can be deposited at 95 °C (43).

Gakis et al. showed that the progression of the very first ALD cycles (< 25), of Al_2O_3 on H-terminated Si (100) substrate, can be modeled with the geometric growth aspects, disregarding the changes in surface reactivity. This growth model is significant in understanding and controlling very thin films(44).

The production of a highly electrochemical stable nanolaminate anode for lithium-ion batteries using ALD was described by Cao et al. in 2019. The group deposited ZnO and TiO_2 alternatively, on a copper foil, through 24 full cycles compromising 26 half-cycles for each oxide. They found a charge capacity over 600 $mAh\,g^{-1}$ (45).

In 2020 Cao et al. demonstrated that it is possible to achieve a high photocatalytic activity, under visible light, by depositing Fe_2O_3 via ALD on commercially available TiO_2 powder with only 400 cycles. They managed to obtain over 95% methyl orange degrada-

tion in 90 min (46). This leads to the consideration that cycles in the thousands, or lower, range might be optimal for achieving some electrochemical proprieties without creating an effective metal oxide insulation barrier.

The morphology of the substrate, porosity, tortuosity, etc., can affect the final deposited layer microstructure. This has been demonstrated by Trought et al. , they used different morphologies and densities of functional sites, produced by etching a carbon substrate (highly oriented pyrolytic graphite) with different acids, to show that these two variables can affect the nucleation of deposited Al_2O_3 deposited through ALD (47)

However, ALD is not restricted to ceramic or metallic substrate, there are studies on atomic layer deposition employed over polymeric materials. An et al. have thoroughly reviewed the process of supersonic spraying at near ambient temperature, including coating of polymeric nanofibers with reduced graphene oxide, which can be tuned for many applications such as sensors and water-based photoelectrodes (48). While Darwish et al. successfully coated poly (methyl methacrylate) (PMMA) through ALD at low temperature (65 °C) with a thin film of TiO_2 and achieved a water contact angle 90% lower than the uncoated PMMA (49). For some in-depth review of the ALD process I highly recommend the references: (8, 16, 20, 26, 50).

One of the differences between depositing on a non-woven pyrolyzed fiber and the nanocellulose is the reactive groups at the surface. As explained by Norrrahim et al. BNC has a high concentration of hydroxyl groups, -OH, that enables easy functionalization of nanocellulose (51). Kynol fibers are pyrolyzed at high temperatures (> 700 °C) and during this process hydroxyl and methylol groups and noncyclic groups are lost. These Kynol carbon fibers contain proportionally less hydrogen and oxygen, as low as 5% in weight (52), when compared to bacterial nanocellulose which has around 55% of hydrogen and oxygen, in weight, or 5 OH per nm^2 (53). That is one of the reasons why BNCs are effectively more reactive and very attractive for ALD process.

Applying ALD to nanocellulose is, however, not new, in 2014 Habibi reported it a summary of the advances in the chemical modification of nanocelluloses (54). In an efficient review of nanocellulose oil sorbents, Liu et al. includes ALD as a commonly used hydrophobization process of cellulose-based aerogels (55). It has also been found that BNC coated with aluminum oxide via ALD may present an excellent sorption of fluoride ions, with a maximum adsorption of fluorine at only 50 nm layer thickness (56).

Among several applications, ALD coated BNC-derived carbon aerogels can be used as lightweight capacitor electrodes. The main advantage of capacitors is their ability to deliver electrical energy, previously stored, at speeds much greater than those of conventional batteries. This delivery occurs through an applied potential to two plates (electrodes), separated by a dielectric material, on which the electrical charges will accumulate. In the case of electrochemical capacitors, the ions of an electrolyte solution will flow to one plate or the other, depending on their charge (9). Carbon is one of the most used materials as an electrode in electrochemical capacitors because it meets the requisites of good conductivity

and electrochemical stability (9, p. 68-77, 57). However, what will distinguish the different forms of carbon, and thus their electrochemical properties, are two key characteristics: specific surface area (SSA) and open porosity (57). These two characteristics are both present in BNC.

Several studies have applied ALD on mesoporous substrates (58, 59), in special carbon ones; however, most of them start off with carbon-ready substrate or nonbacterial cellulose. I aim to process pyrolysis and heat treatment simultaneously, similar to the approach of Ma et al. (60). This paper explores, therefore, BNC, a natural polymer, and nonwoven carbon (Kynol), two 3D interlock fibers' structures, as a carbon source, when subjected to atomic layer deposited titanium oxide with potential application as electrodes for capacitors.

Li et al. used a combination of ALD and heat treatment to examine the sticky-hydrophobic wetting behavior of cellulosic paper. Trimethylaluminum (TMA) was used as precursor and water as coreactant. They have found that, upon heating to $150\,°C$ in air, with only one single ALD cycle the paper undergoes from a hydrophilic to sticky superhydrophobic transition (61).

The photocatalytic activity and antibacterial activity of TiO_2 and ZnO films deposited onto polyamide (PA-66) fabrics were investigated by Akyildiz et al. in 2021. They have found that ZnO films were more effective in annihilating Staphylococcus aureus bacteria than TiO_2 but also that the fabric sample coated with 10nm ZnO, when exposed to solar simulator four hours, decreased the methylene blue concentration in 68% (62).

3.2 BACTERIAL NANOCELLULOSE

As the name suggests, cellulose comes from the cell; it is a natural polymer found on the cell wall of green plants (*Viridiplantae*). It is, therefore, the most common and abundant polymer on our planet, and it should be no surprise that, in different manners, cellulose takes part in human life (63). In-depth studies on the cellulose structure were vital in developing polymer and macro-molecules science. Though decades after the invention of the first thermoplastic polymer, the celluloid (63, 64).

Bacterial cellulose is very similar to those produced by plants; it is, however, extra-cellular, highly pure, and does not contain other components such as lignin (63). Lignin removal is a crucial and intensive step in the vegetable cellulose purification process. The lack of lignin in the bacterial cellulose means that this step is unnecessary, thus facilitating its processability when compared to plant base cellulose (3).

Studies on bacterial cellulose have been done since the late eighteen hundreds, especially the cellulose synthesized by the bacillus *Gluconacetobacter xylinus* (65, 66). After the publication of the first mechanical proprieties for this and other bacterial cellulose, it caught the attention of more researchers and engineers (3).

Figure 9 – Fiber scale diagram
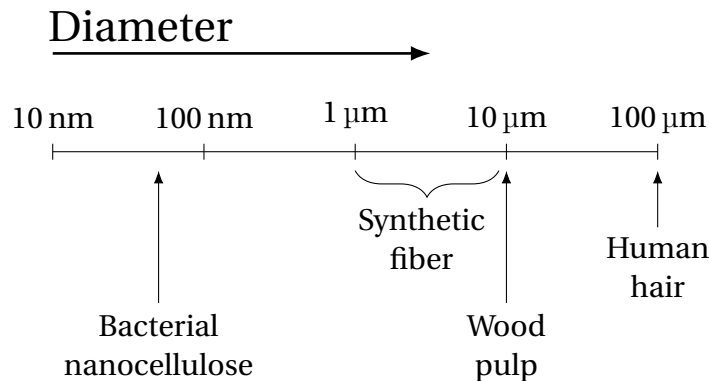
Source: Author, inspired by (71).

These bacteria synthesize the cellulose from a carbon source, like sugars, which are later transformed into glucose and eventually extruded through pores on the bacteria cell wall. Some bacteria contain special enzymes that help with the formation of cellulose. Passing through this extrusion process, the glucose self-organizes into microfibrils that later pack to a bundle to be cellulose (67).

The macroscopic synthesis of bacterial cellulose may occur in two forms of the medium; static or agitated. Under the static mode, the bacterial will produce a cellulose layer in the interface between air and the medium. Such a layer tends to thicken with time. Under agitation, the bacteria will form this layer in all directions as it bounces, thus giving shape to a spherical cellulose film. Other important factors that may influence cellulose growth are; temperature, pH of the medium, type of carbon source, surface area in contact with oxygen, and amount of oxygen available (68, 69). The precise reason why these bacteria produce such cellulose is unknown. Some authors suggest this is a form of protection from the environment, principally UV light. Others point out that it would be a way to keep itself closer to its nutrients and oxygen source (in aqueous) (3).

The cellulose nanofiber structure created by the bacteria is very promising as a matrix for gelation because it redistributes mechanical stress and allows for a wide variety of shapes and fiber density gradient (3, 68). Bacterial cellulose fibers usually have a diameter between 40 nm to 70 nm, as displayed in Figure 9 relative scale size of fibers, (67, 70).

3.2.1 BNC State of the Art

This subsection provides a view of some of the state of the art of nanobacterial cellulose research. Among the many papers published from 2017 to 2021, one of the highlights is by Parte et al. reviewing the production process of BNC. In this recent review of the production process of BNC, Parte et al. discuss some different bioreactors shapes and agitation methods together with their BNC shape results. It is a highly valuable review of the

growth limitations, parameters, and media of BNCs, useful for large-scale industrial production (72). Rühs et al. in 2018 indicated a direct method for producing three-dimensional BNC with controlled macroporosity by foaming the media with mannitol accompanied by a stabilizer (Cremodan) and a viscosity tuner (Xanthan) (73).

A general review, and some new findings in the major field of BNC, biomedicine and biotechnology, are presented by Swingler et al. Despite the recognizable biocompatibility of BNC, only a few studies have been conducted in humans (in vivo) (74) thought with promising results for recovering depth of the ulcers (75). Another interesting case study was an attempt to restore the tympanic membrane (eardrum) using BNC patch (76).

In 2019, Gao et al. demonstrated a technique for growing, through the use of a functionalized glucose under the method of *in situ* microbial fermentation, a fluorescence BNC. Confirming that BNC (K. sucrofermentans) can metabolize modified glucose (77). This is of special importance because it may open the door to incorporating many different compounds directly by feeding the bacteria.

3.3   ELECTROCHEMICAL CAPACITOR

Capacitor and batteries are both electronic components capable of holding charges. The main difference is for how long they can keep the charge after the electric field is removed and also how fast it can deliver this charge.

A conventional capacitor consists of two parallel plates, usually made of metal (electrodes), usually separated by an insulating (dielectric) material such as polymers or ceramics. When the metal plates are connected to an external circuit capable of applying a potential difference, in a direct current regime, electrons begin to flow to one plate, and opposite charges accumulate on the surface of the other plate until the charges reach equilibrium (9, p.69-73). This is illustrated in the Figure 10.

The ability of a capacitor to store charge (Q), at a given electrical field, established by the potential difference (V) between each plate , is called *the capacitance* (C) as follows (9, p.70):

$$C = \frac{Q}{V} \tag{4}$$

Charges of the same polarity on one plate are mutually repelled while also attracted to charges of opposing polarity, and these charges accumulate at the surface of the opposite plate. Therefore capacitance is directly proportional to the surface area of the electrodes. Other factors influencing it are the dielectric material used, and the distance between the electrodes (9, p.71).

Electrochemical capacitors, also known as supercapacitors, have the *double layer* formation; the charges of an electrolyte flow freely and accumulate at the surface. These are sometimes referred to as electric double-layer capacitors (EDLC). The first layer is directly at the surface, while the second layer (also known as Helmholtz Layer) is composed of ions from the electrolyte. This double layer yields a much higher capacitance, over four times the order of magnitude of conventional capacitors; hence the name *supercapacitor* (9, p.71).

Electrochemical capacitors are subject to other factors which influence their capacitance, such as the accessibility to the electrode surface, as displayed on Figure 12, and the electrolyte proprieties. Depending on the size of the ions, a nanometric pores might become covered by the second layer in a manner such that the ions in another layer - the diffusion layer - might encounter a different surface area. As explained by Beguin et al.:

> The movement of electrolyte ions within the pore network of EDLCs will experience varying degrees of mass transfer limitations associated with confined pores, the tortuous path through the carbon material, pore lengths, and ion sieving / exclusion effects at pore openings; particularly openings that approach, or are smaller than, the size of the solvated electrolyte molecules [...]. Hence, not all the surface of the porous electrode will be accessed by the electrolyte in the same time frame and, therefore, upon discharge, the rate at which the capacitance can be delivered will also vary. (9, p. 76-77)

The capacitance is usually measured, at laboratory scale, by a technique called *Cyclic voltammetry*. It consists of applying a linear voltage ramp to an electrode-cell assembly, that varies between two voltage boundaries, and then measuring the resulting current (9, p.116). The speed at which the voltage changes from the initial to the final

boundary (or the slope of the ramp) is the *sweep rate* (mVs^{-1}) as illustrated in Figure 11. The capacitance can be calculated from the cyclic voltammetry by the area of the formed curve as follows (9, p.117):

$$C = \frac{\int_{V1}^{V2} i \, dt}{\int_{V1}^{V2} V \, dt} \tag{5}$$

where C is the capacitance, $V1$ and $V2$ are voltage boundaries, i the current and V the voltage.

For an in-depth review of the differences between this measurement and others, refer to the evaluation done by Palagonia et al. (79).

Pseudopacitors, have the faradaic effect of the *redox reactions* between electrodes and electrolyte, unlike conventional capacitors and pure double layer capacitors (81). The so-called hybrid capacitors have the redox reaction and double layer effect, which is only partially reversible. For a comprehensive review on supercapacitors and recent findings, refer to Poonam et al. (82).

The capacitance depends on the surface of the electrode. In the case of deep micropores, the *necessary time for the ions to access this area* will be longer than for external surfaces. When high-frequency currents are applied, they might not access such areas. The outcome is that with increasing signal frequency, the capacitance amplitude diminishes (9, p.375). As described by Beguin et al.:

" At high frequency, the deep [···] surfaces are no more accessible because the ions moving in the electrolyte do not have the time to reach them. Consequently, the ions will neither contribute to the current transport nor the ohmic losses." (9, p. 375)

Another important concept is the *electrical impedance*. Electrical impedance is the opposition to a electric current presented by a electric circuit, or component, through two effects; resistance and reactance (83, p.5). The reactance is "an additional opposition to the movement of electric charge that arises from the changing magnetic and electric fields in circuits carrying alternating current" (84).

Figure 10 – Conventional capacitor schematic.
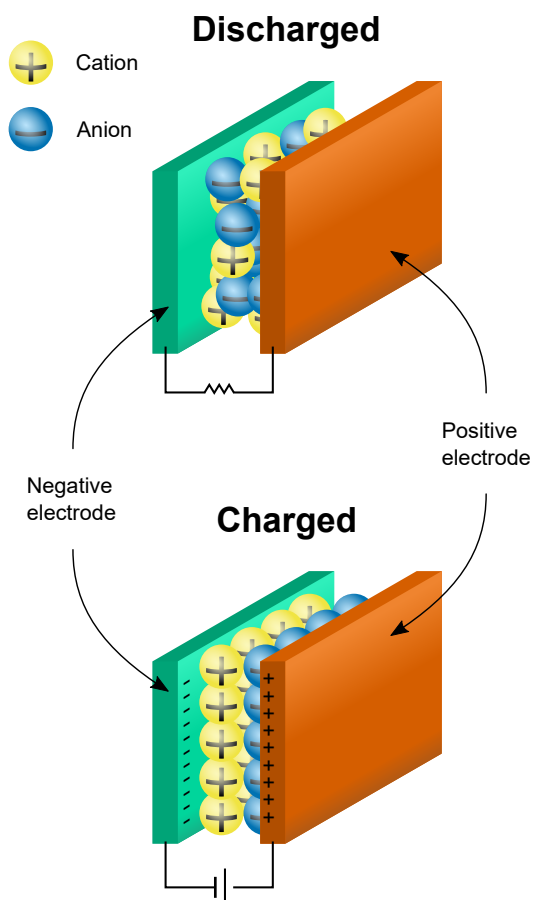
Source: Author, inspired by (78).

Figure 11 – Cyclic voltammetry.
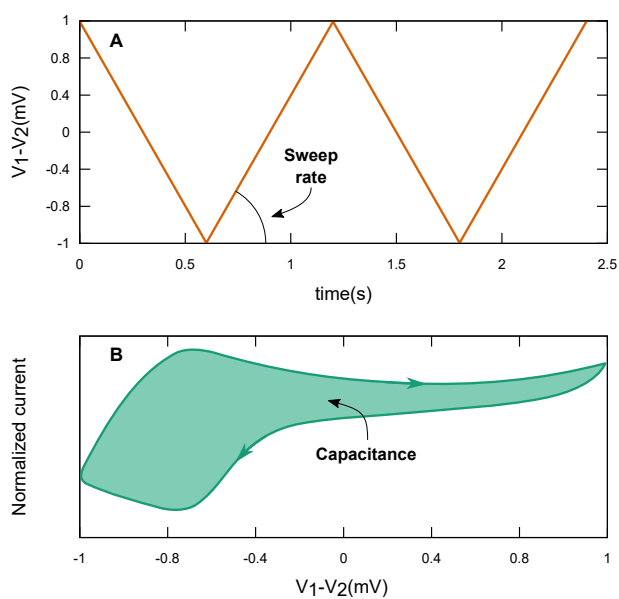
In **A** Potential versus time with the indication
of the Sweep rate (slope), in **B** Cyclic voltam-
metry with curve area highlighted.
Source: Author, adapted from (80).

Figure 12 – Doublelayer capacitor schematic.
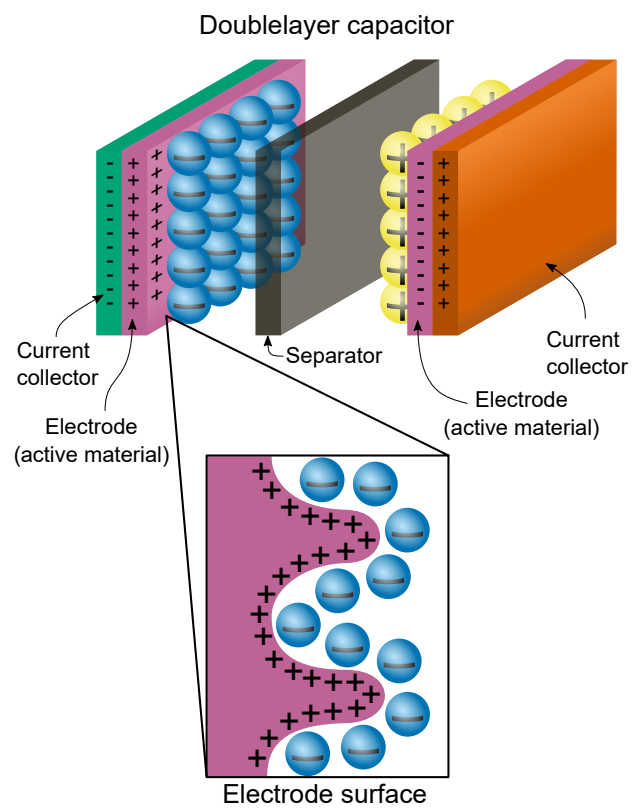
Source: Author, inspired by (78).

4 Materials and Methods

"Oh, no, sir! I can't always sleep. Though I've no great pain, still I've an ache, there,—right inside,—and in my bones too; it won't let me sleep as I ought. No; but there, I lie by myself; I lie here and lie here, and don't think: I feel that I'm alive, I breathe; and I put myself all into that. I look and listen. The bees buzz and hum in the hive; a dove sits on the roof and cooes; a hen comes along with her chickens to peck up crumbs; or a sparrow flies in, or a butterfly—that's a great treat for me. Last year some swallows even built a nest over there in the corner, and brought up their little ones. Oh, how interesting it was!"

Ivan Turgenev, 1917, A Living Relic.

4.1 SAMPLES PREPARATION AND DEPOSITION

4.1.1 Samples

The first substrate were obtained from Bacterial nanocellulose thick membranes. These membranes were synthesized by the bacteria *Gluconacetobacter Xylinus*, following the procedure described in (85) (for a brief description see Subsubsection 4.1.1.1 *BNC preparation* at page 47). The generated BNC was then dried, both stages, wet and dry, are shown in Figure 13b.

The second substrate was a highly porous and high specific-surface-area activated carbon (95%) nonwoven textile ACN-211-20 (Kynol Europa GmbH) called in this thesis simply as *Kynol*. These commercial fibers are derived from a three-dimensional cross-linked phenolic resin (52). Samples were cut into $1\,\text{cm} \times 1\,\text{cm}$ pieces and used as received, without additional treatment, as seen in Figure 13c.

Figure 13 – Sample's photography

(a)

(b)   (c)
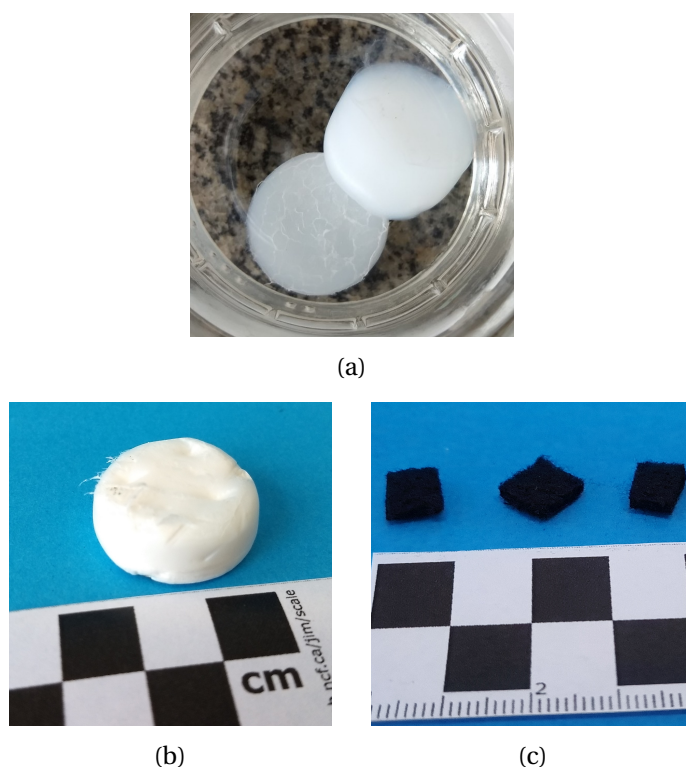
In (a) BNC hydrogel, in (b) BNC aerogel sample after supercritical drying. In (c) Kynol nonwoven samples cut into $1\,\text{cm} \times 1\,\text{cm}$ pieces.
Source: Author.

4.1.1.1 *BNC preparation*

The BNC synthesis process was as follows: the bacteria were grown inside a Falcon tube for several days until the hydrated nanocellulose layer had reached 1 cm height. Next, the bacteria were removed from the formed 3D structure using NaOH (100 mmol) at 50 °C for 24 h, and the cellulose was rinsed with distilled water (85). The nanocellulose hydrogel, see Figure 13a, passed through a solvent exchange, from water to ethanol, consisting of five progressive exchanges during two days. The ethanolic gel was then super-critically dried, with three cycles of CO_2, using an Autosamdri 931 (Tousimis) supercritical drier, which resulted in *nanocellulose aerogels* that maintained their structure.

A summary of this processing steps is displayed in Figure 14. These were later cut into small chunks of approximately $0.5\,\text{cm} \times 1.0\,\text{cm}$. These processing steps, namely supercritical drying, were combined with a pyrolysis step – later described, to achieve a carbon structure comparable to the nonwoven activated carbon.

Figure 14 – BNC drying stages
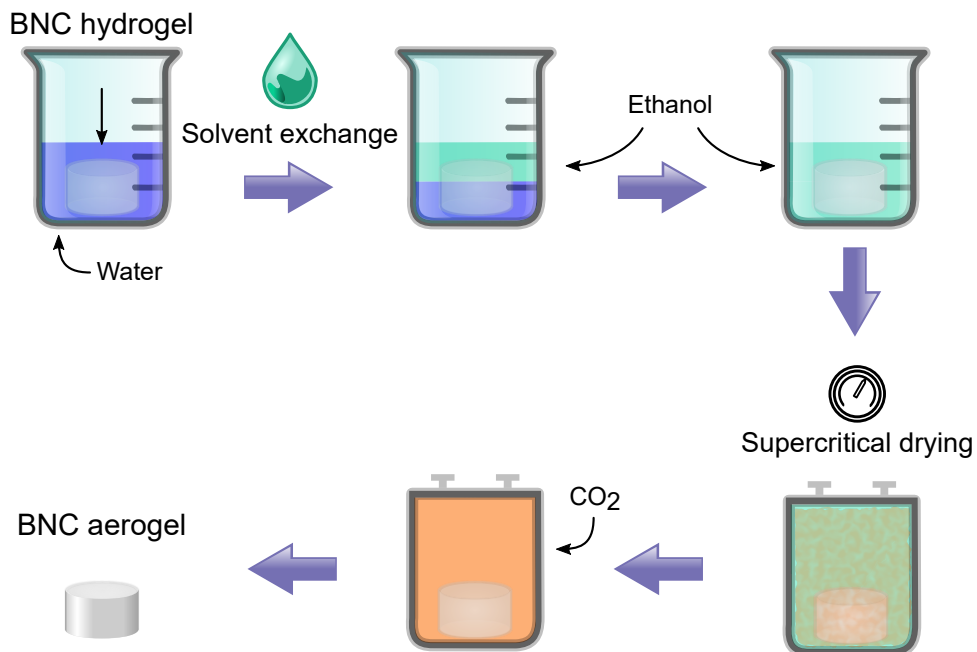
Drying steps of the BNC hydrogen to aerogel.
Source: Author.

4.1.2 Deposition

Atomic layer deposition was carried out in a homemade reactor (Hamburg University of Technology, Institute of Advanced Ceramics – Integrated Materials Systems Group) under exposure modes at a low temperature of 95 °C using nitrogen as the carrier gas (30 sccm).

For the deposition titanium oxide was chosen due lower toxicity when compared to $TiCl_4$ (16). The precursor used was TIPP (Sigma Aldrich) and deionized water as co-reactant. Both samples were subjected, separately, to two different ALD processes comprising of 700 cycles.

Figure 15 displays the process scheme of the gas flow sequence in and out of the chamber, including the exposure time. TIPP and water's pulse/exposure/purge time were 1/30/60 and 0.1/30/90 seconds, respectively as displayed in the Table 3.

Table 3 – ALD Cycle times

	Steps	Time (s)	
		TIPP	Water
Full Cycle	Pulse	1	
	Exposure	30	
	Purge	60	
	Pulse		0.1
	Exposure		30
	Purge		90

Time in seconds.
Source: adapted, with permission, from Graciano B. De Souza et al. in Advances in Materials Science and Engineering ©① Hindawi (1).

Figure 15 – ALD time-steps cycle plot
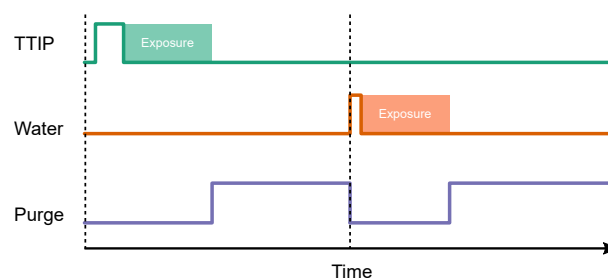
ALD time-steps cycle plot with each precursor pulse, exposure, and purge steps over time.
Source: adapted, with permission, from Graciano B. De Souza et al. in Advances in Materials Science and Engineering ©① Hindawi (1).

Due to the samples' highly porous and low-density nature, a large-mesh stainless-steel dome was built within the chamber to protect the samples and avoid displacement during the precursors' pulse. On each process, a total of 8-10 samples were accommodated in the reactor. A piece of a commercial silicon wafer (as received, `<100>`, Si-Mat silicon materials) was placed inside the chamber next to the samples to estimate the equivalent

layer thickness after deposition. These silicon wafer pieces' layer thickness were analyzed using a spectroscopic ellipsometer (SE-2000, Semilab Semiconductor Physics Laboratory Co. Ltd.) using Tauc-Lorentz dispersion law, with a wavelength range between 450.06 nm to 974.66 nm, and an angle of incidence of 70.12°.

4.1.3 Post-processing

After the ALD deposition, the BNC aerogel was subjected to a pyrolysis process under N_2 atmosphere, with a heating rate of $10\,°C\,min^{-1}$ until the plateau temperature of $800\,°C$, which was held for two hours. A Kynol sample was burned on a muffle furnace using a heat rate of $10\,°C\,min^{-1}$ until the plateau temperature of $400\,°C$, which was held for two hours for scanning electron microscope inspection. The Kynol samples used in the electrode assembly were not heat treated.

4.2 CHARACTERIZATION

4.2.1 Microstructural

For a visual evaluation of the microstructural evolution of the samples, Scanning electron micrography (SEM) (Zeiss Supra VP 55) was used before and after each stage. The samples were analyzed in four different states:

1. Before deposition

2. After deposition

3. After pyrolysis (BNC)

4. After burn-out (Kynol)

The burned-out state was used to analyze the ALD coating in detail. After attaching the samples to a conductive carbon tape on an appropriated metal stub, they were subjected to a gold sputter deposition process with 40 mA for 30 seconds under argon flux.

The phases were characterized by X-ray diffraction (XRD) performed with a Rigaku MiniFlex X-ray diffractometer, using a copper source (λ Kα 1.540 5 Å), with $10\,°\,min^{-1}$, and a step time of 0.02 s. Phase identification was carried out with the software QualX (v2.24) and Profex (v4.3.5) (86, 87). The anatase spectrum was refined using Rietveld method.

The carbon structure of the Kynol sample was further investigated by Raman spectroscopy with the innoRam (B&W TEK) spectrometer, using a 532 nm wavelength green laser.

4.2.2 Textural

For the Specific Surface Area (SSA) evaluation, the samples were first subjected to a vacuum degassing, for 2 h under 120 °C, to remove humidity and other adsorbed species, despite the recommendation of 8 h (88, p.239), due to laboratory usage restrictions at the time. Because of availability, nitrogen (90%, White Martins) was used as absorbent gas. The adsorption analysis using the Surface area via Brunauer Emmett Teller (S_{BET}) method was carried out in a Quantachrome Nova 1200e equipment, with anti-elutriation filter on the sample holder, operated at 77 K, using 240 seconds as thermal equilibrium timeout.

4.2.3 Electrochemical

The electrodes used for the electrochemical characterization were produced by coating an aluminum plate with a slurry of the active material sample (BNC or Kynol). In order to accomplish that, the samples were ground into a fine powder using an agate mortar and pestle, then added to a Polyvinylidene DiFluoride (PVDF) and N-Methyl-2-pyrrolidone (NMP) solution, with the following WP of `10:1:1000` as displayed in Table 4 and thoroughly mixed using a vortex vibrator.

Table 4 – Electrode slurry WP

Function	Material	WP (%)
Active material	Carbon	10
Binder	PVDF	1
Solvent	NMP	1 000

Source: Author.

The prepared slurry was applied to the aluminum plate carefully using a spatula and then dried at 120 °C for six hours. A simplified scheme of the electrode assembly is displayed in Figure 16. The electrochemical properties were measured using a Metrohm potentiostat (Autolab PGSTAT204 FRA32M) coupled with Nova 2.0 software. A two-electrode setup was employed for these measurements, with a high-purity Pt as counter electrode in 1 mol KOH solution. The Cyclic Voltammetry (CV) curves were performed at scan rates between 5 mV s^{-1} to 100 mV s^{-1}, while the impedance was measured between 100 kHz and 0.001 kHz.

The Specific Capacitance (C_p) was calculated from the area of the CV curves, using Equation 6:

$$C_p = \frac{A}{2k\,m\,\Delta V} \tag{6}$$

where A is the integrated area from the voltammetry curve, k is the voltage sweep rate, m is the mass of the electrode, and ΔV is the voltage range.

Figure 16 – Schematic of the electrode assembly steps
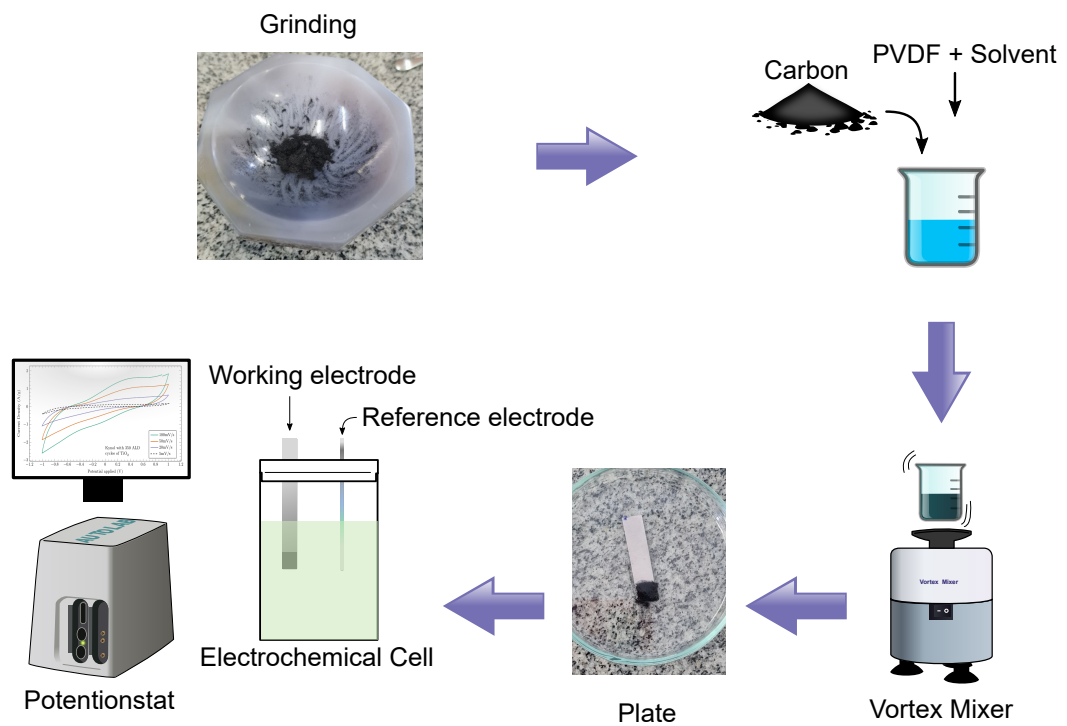
Grinding

PVDF + Solvent

Carbon

Working electrode

Reference electrode

Electrochemical Cell

Potentionstat

Plate

Vortex Mixer

 Source: adapted, with permission, from Graciano B. De Souza et al. in Advances in Materials Science and Engineering ©① Hindawi (1).

5 Results and Discussions

"All theory is gray, my friend. But forever green is the tree of life."

Johann Wolfgang von Goethe, Faust, First Part I

5.1 ELLIPSOMETRY

In order to evaluate the performance of the ALD process itself we measured the TiO_2 layer thickness indirectly, on the silicon wafer pieces, as displayed in Table 5. These results indicate that the deposition occurred normally. Our findings are very close to those found by Skopin et al., for 2 seconds exposure of titania deposition on silicon substrate (89).

Table 5 – TiO_2 layer thickness ellipsometry

Sample	Thickness (nm)	Fit (R^2)
BNC 700	17.8	0.982 57
Ref. (89)	20.4[*]	
Kynol 700	21.4	0.999 4

Layer thickness on Si wafer.
[*] Extrapolated from the value of 5.4 ± 1.1 for 185 cycles.
Source: adapted, with permission, from Graciano B. De Souza et al. in Advances in Materials Science and Engineering ⓒⓘ Hindawi (1).

5.2 MICROSTRUCTURAL CHARACTERIZATION

SEM of the Kynol and Nanocellulose samples is shown in Figure 17, where the original morphology of the fibers is preserved after the ALD with titania. In Figure 17A (25k magnification) the bacterial nanocellulose fibers appears entangled, branching into various directions, and several nanometers distant from one another, similar to previous studies (77, 90). In Figure 17C (500X magnification) the Kynol fibers display more straight pattern, also equally far apart from each other, resembling the findings of Lee (91). As expected from ALD processing, no defects were identified in the coatings (Figure 17B and D), pointing out a uniform layer.

In Figure 18 presents SEM and particular zoomed images of the samples after pyrolysis (in nitrogen), or burnout (in air), that all samples are still highly porous, even though morphological alterations are present. For the nanocellulose pyrolyzed samples (Figure 18A and B), sintering of the fibers is observed, with the formation of spider-net-like structures. Former publications by our group (43) regarding ALD-based TiO_2 inverse opals with nanometric features have shown that sintering is quite pronounced for such nanostructures, leading to complete destabilization and formation of a vermicular structure after 900 °C (92).

Interestingly, the nanocellulose samples (Figure 18 A and B), heat-treated in nitrogen, present a different morphology, where the original fibers are enlarged in size, pointing

Figure 17 – SEM morphology comparison

In A uncoated and B after TiO_2 coating by ALD, in C Kynol uncoated fiber, and
D Kynol after TiO_2 coating.
Source: adapted, with permission, from Graciano B. De Souza et al. in Advances in Materials Science and Engineering ©① Hindawi (1).
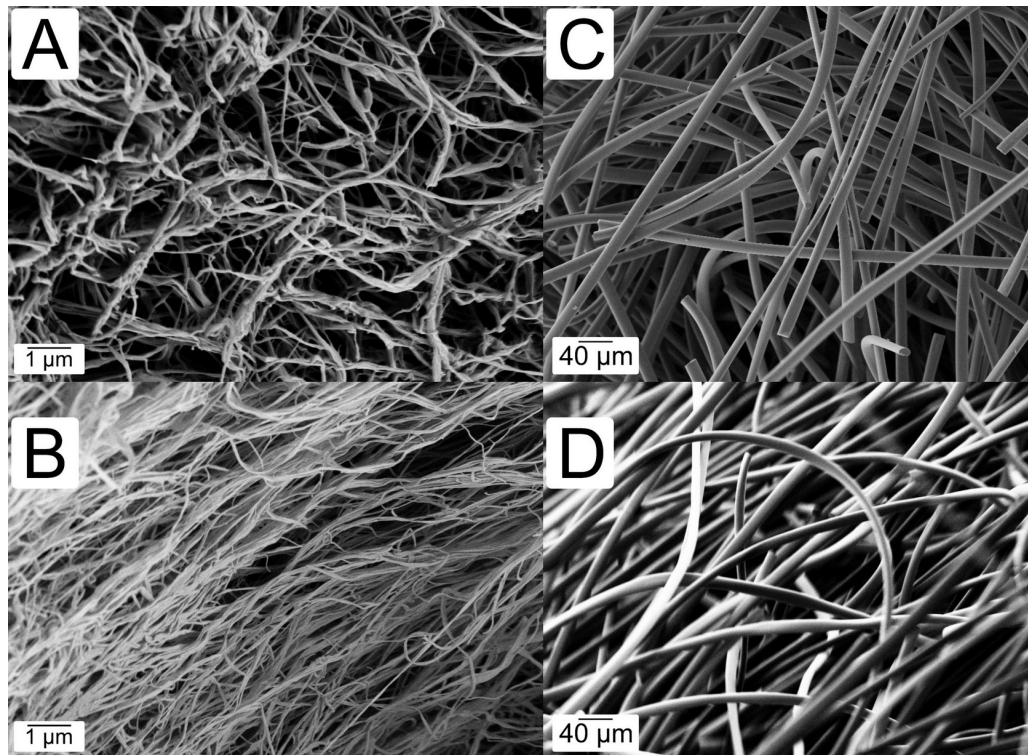
out a potential grain growth within the coating. For the Kynol samples (Figure 18C and
D), heat-treated in air, a squished straw-like tubular shape is observed, also with enlargement compared to the non-coated fiber. This hollow structure was expected since the heat
treatment occurs in air and thus the carbon fraction was burned away, similar to the results
found in (86). The thickness observed in Figure 18D may have been extended by the gold
sputtering.

Figure 18 – SEM comparison of TiO$_2$ ALD samples after heat treatments
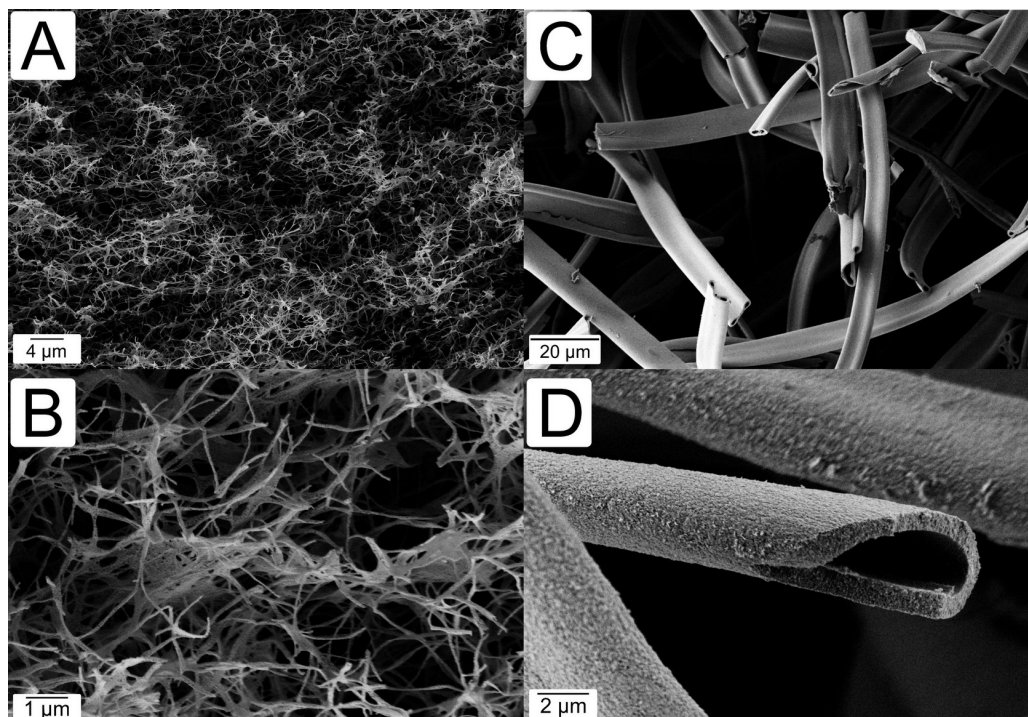
Structural morphology of TiO$_2$ ALD-coated nanocellulose samples after pyrolysis on A and B. On C and D, the morphology of TiO$_2$ coated Kynol samples after burn-out in air, where a straw-like structure can be seen.

Source: adapted, with permission, from Graciano B. De Souza et al. in Advances in Materials Science and Engineering ⓒⓘ Hindawi (1).

5.3 PHASE IDENTIFICATION AND EVOLUTION

5.3.1 Raman phase identification

The Raman spectroscopy measurements of the Kynol samples prior to deposition (Figure 19) shows the expected carbon related D and G bands at $1\,335\,\mathrm{cm}^{-1}$ and $1\,604\,\mathrm{cm}^{-1}$, respectively (93, 94). The broad G band at reveals the existence of more disorder carbon than graphitic sheets present in the material. The ID/IG ratio we found was 0.917, which is very close to what was found by Lee, 0.92, for another similar activated carbon textile from the same manufacturer (91). This high ID/IG ratio is usually associated with high temperature processing, pyrolysis but not graphitization (95)

Figure 19 – Kynol Raman spectroscopy

Kynol Raman spectroscopy in **(a)** and zoomed in **(b)** with D and G bands highlighted.
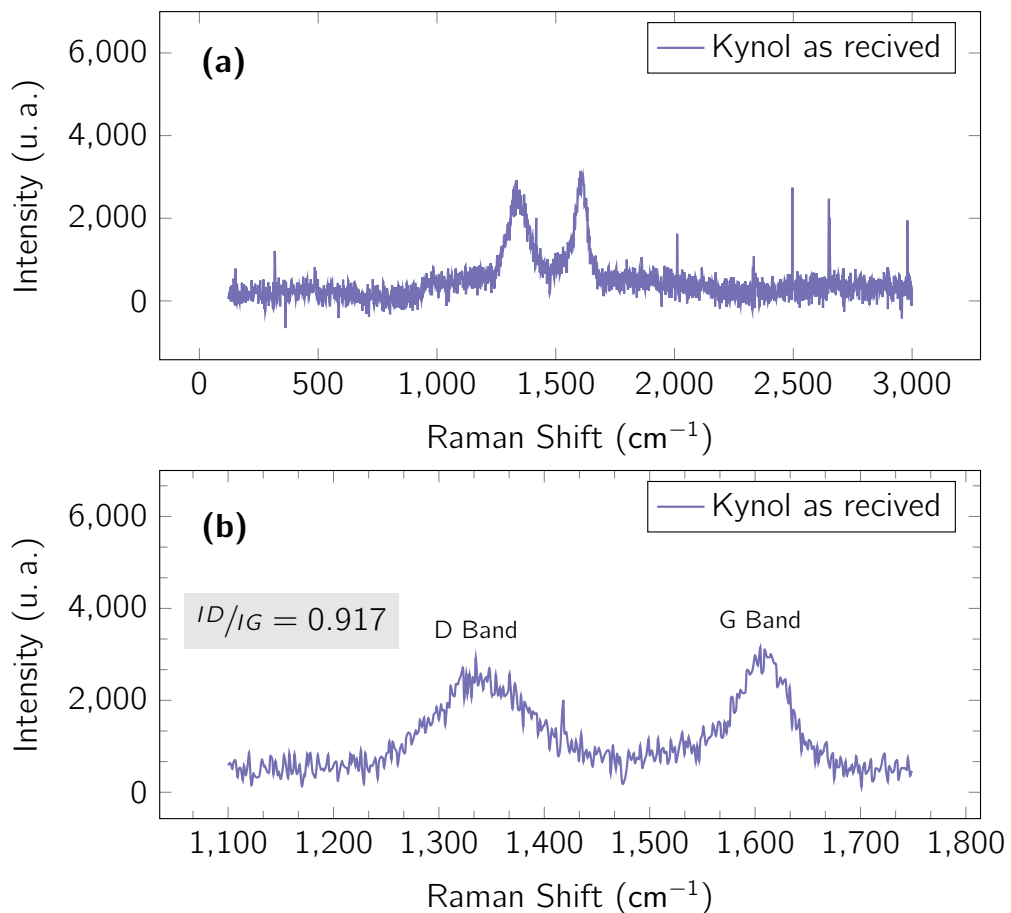Source: adapted, with permission, from Graciano B. De Souza et al. in Advances in Materials Science and Engineering ⓒⓘ Hindawi (1).

5.3.2 XRD phase identification and evolution

The Kynol sample coated with TiO$_2$ ALC-coated Kynol sample, Figure 21d and 21e, shows a predominantly amorphous curve, with some peaks related to TiO$_2$ anatase phase peaks identified at 47.84°, 53.53° and 54.86° (ICSD 009854). The broadbands centered around 23.92° and 24.57° correspond to carbon phases (ICSD 28417 and ICSD 28419) (96, 97). A similar result has been found by Rahmawati et al. with similar carbon substrate and TiO$_2$ deposition (98).

The TiO$_2$ ALD-coated nanocellulose samples, Figure 21a, 21b, and 21c, show peaks at 16.8° and 22.7°, corresponding to crystalline cellulose (CCDC pattern num. 1866391) (99). No titanium carbide (TiC) peaks, neither at 36.9° and 42.6°, (100, 101, 102) could be observed and thus the formation of such phase was discarded. However, on the pyrolyzed sample (Figure 21c), we see that the cellulose prominent peak remains despite the high temperature. We expected that they would have decreased (103). This remaining peak suggests that the titania layer may have partially protected the fibers, as similar results have been found by other researchers (104) and (105), and partially graphitized due to the appearance of the peaks at 26.2° and 44.3° (ICSD 31170). This result agrees with that published by Li et al. (106).

Finally, several anatase peaks were also identified at 25.2°, 37.5°, 53.53°, 54.86° and 62.3°. and no rutile peaks could be detected. Refinement of the anatase phase, with χ^2 value of 2.25 ($R_{wp} = 4.85\%$), which was considered as acceptable according to (107), indicated a crystallite size of 80±8 nm. The expected phase transition from anatase to rutile (108) did not occur, which could be a result of a conjunction of factors such as crystallite size and particle size (109). We believe that these factors are the most likely to have influenced in our results. Crystallite size and particle size are directly related to the deposition temperature ,which been shown to yield anatase after heat treatment at 900 °C (110), and might have affected the grains.

Henegar et al. have demonstrated that is possible to achieve anatase stabilization through ALD, even after annealing at 900 °C, if the deposition temperature is below 150 °C. They concluded that this is due to the crystallite size and the lower adhesion of the deposited layer to the substrate (111). As the ALD process in this work was set to 95 °C the lower deposition temperature hypothesis is reasonable.

In addition to using a low deposition temperature, 95 °C, Pasquarelli et al. have also evinced that an inverse opal substrate infiltrated via ALD can have its anatase-to-rutile transformation thermally-delayed in air, and inhibited under vacuum, even when heat treated at 1 000 °C for 4 h or 1 300 °C for 3 h under vacuum. They suggest that a highly porous structure could intrinsically hinder phase transformation by spatially limiting particle agglomeration and reducing the number of nucleation sites (43). Other researchers have also investigated further and found similar results (112). A short summary of those findings is presented in Table 6.

Figure 20 – XRD experimental patterns
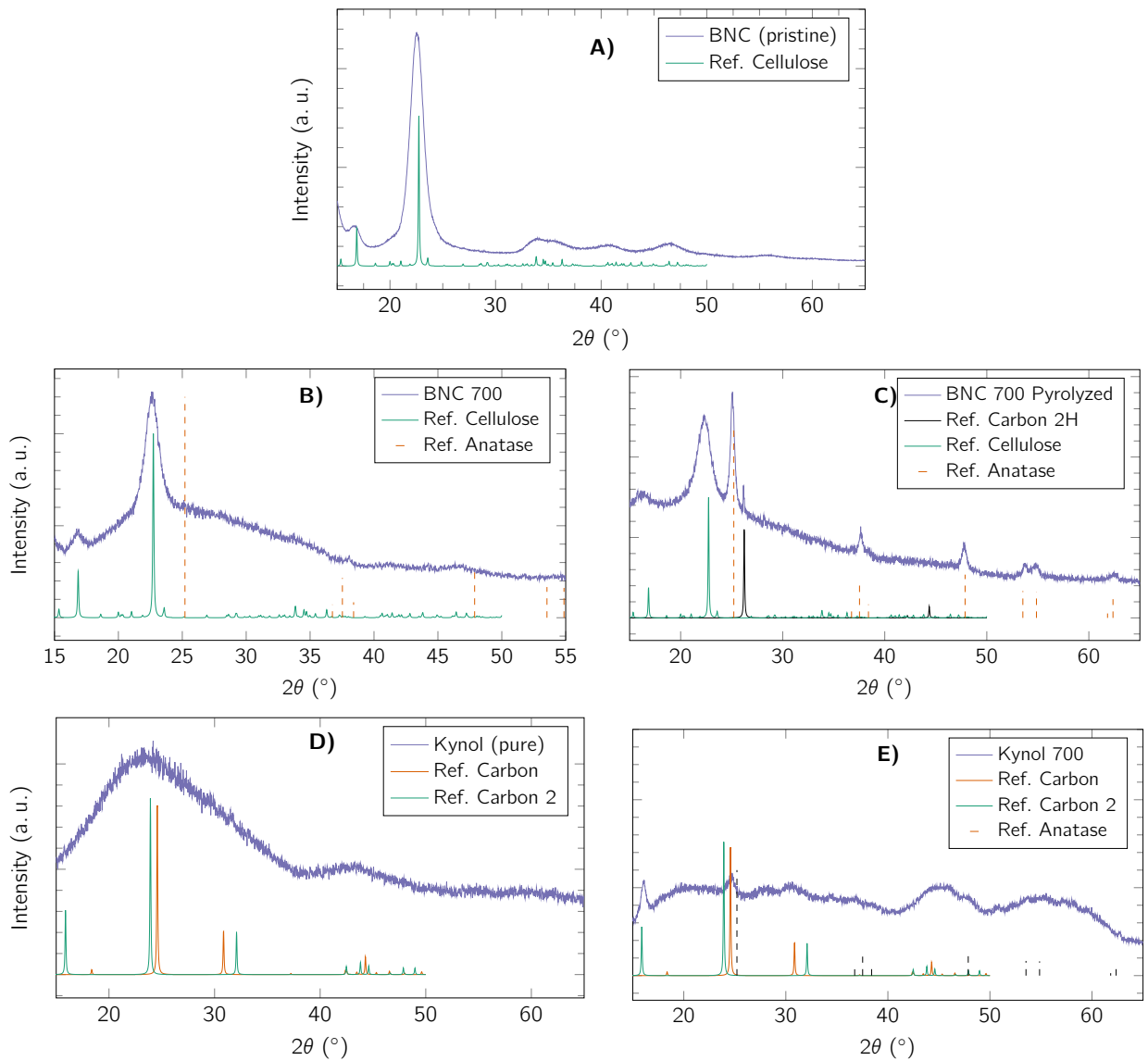
In (a) pristine BNC, (b) TiO_2 ALD-coated BNC, (c) ALD-coated BNC sample after pyrolysis, (d) Pure Kynol, and (e) shows the TiO_2 ALD-coated Kynol.
Source: adapted, with permission, from Graciano B. De Souza et al. in Advances in Materials Science and Engineering ⓒⓘ Hindawi (1).

Table 6 – Summary of anatase-stabilized titania sorted by annealing temperature

Synthesis temp. (°C)	Annealing temp. (°C)	Crystallite (nm)	Standard dev.	Remarks	Reference
23	773	400		Iterative incipient wetness infiltration with intermediate drying at 160 °C.	(112)
95	800	80	8	BNC/Carbon template infiltrated with amorphous titania on low temperature ALD	This work
100	900	200		Native oxide Si 100 deposited via ALD with TDMAT as a precursor	(111)
150	900	90		TiO2 thin film deposited on Si (100) by remote plasma atomic layer deposition (RPALD)	(110)
95	1 000	175	50	Polystyrene template infiltrated with amorphous titania using low temperature ALD	(43)
23	1 000			Titanate nanowires deposited from a suspension via a stamping method	(113)

23 °C was used when report only mention room temperature.
Source: adapted, with permission, from Graciano B. De Souza et al. in Advances in Materials Science and Engineering ⓒⓘ Hindawi (1).

5.4 NITROGEN ADSORPTION

As expected, the BET specific surface area (S_{BET}) decreased with the titania coating. Similar results have been observed for ALD-coated iron oxide nanoparticles (114). While the decrease is slight for the Kynol sample, from $1\,695\,m^2\,g^{-1}$ and $1\,480\,m^2\,g^{-1}$, the difference it is considerable for the nanocellulose sample as displayed in Table 7. This small area indicates a potential non-optimal behavior during the ALD cycle so that instead of individual fiber coating, severely agglomerated fibers are coated as one single piece of material (114). The relatively lower area of the BNC could also be attributed to the sample's structural deformation during manipulation and cutting. The increase in specific surface area (SSA) for the pyrolyzed nanocellulose, $175\,m^2\,g^{-1}$, is associated with probable fiber breakout and coating delamination, as observed in the SEM images (see Figure 18) and some structure loss.

Table 7 – Samples BET specific surface area

Sample run	S_{BET} $(m^2 g^{-1})$	Correlation coefficient (r)
Kynol (pure)	1 695.27	0.999 519
Kynol 700	1 480.97	0.999 588
BNC (pristine)[*]	200	-
BNC 700	50.99	0.999 688
BNC 700 Pyrolyzed	175.65	0.991 937

[*] Reference (115).
 Source: adapted, with permission, from Graciano B. De Souza et al. in Advances in Materials Science and Engineering ©① Hindawi (1).

The S_{BET} tends to decrease as the titania layer thickness increase because the pores are the distance between the fibers. The pyrolyzed nanocellulose shows an increase in SSA probably due to fiber breakout and some structure loss. The relative lower area of BNC samples after deposition correlates to the fiber density observed in the SEM images, this may be attributed to the sample deformation during manipulation and cutting.

5.5 ELECTROCHEMICAL CHARACTERIZATION

Figure 22 shows the CVs of the samples in specific gravimetric current density. The pyrolyzed BNC sample (Figure 22a) shows a more pseudocapacitance curve, while the Kynol sample (Figure 22b) is much less pronounced. The pyrolyzed BNC plot also suggests a less reversible process when compared to the Kynol sample.

As explained by Ntakirutimana et al., at the initial low scan rates (5 mV/s and 20 mV/s), the ions probably have time to completely diffuse into a porous structure, resulting in a greater contact between the electrolyte and the inner surface of the electrode,

and by consequence a larger capacitance (117). However, at higher scanning rate there maybe not enough time for a complete diffusion of electrolyte ions and penetration of the charges into the internal structure of the electrode, which in turn results in smaller capacitance (116).

Figure 22 – Cyclic voltammetry
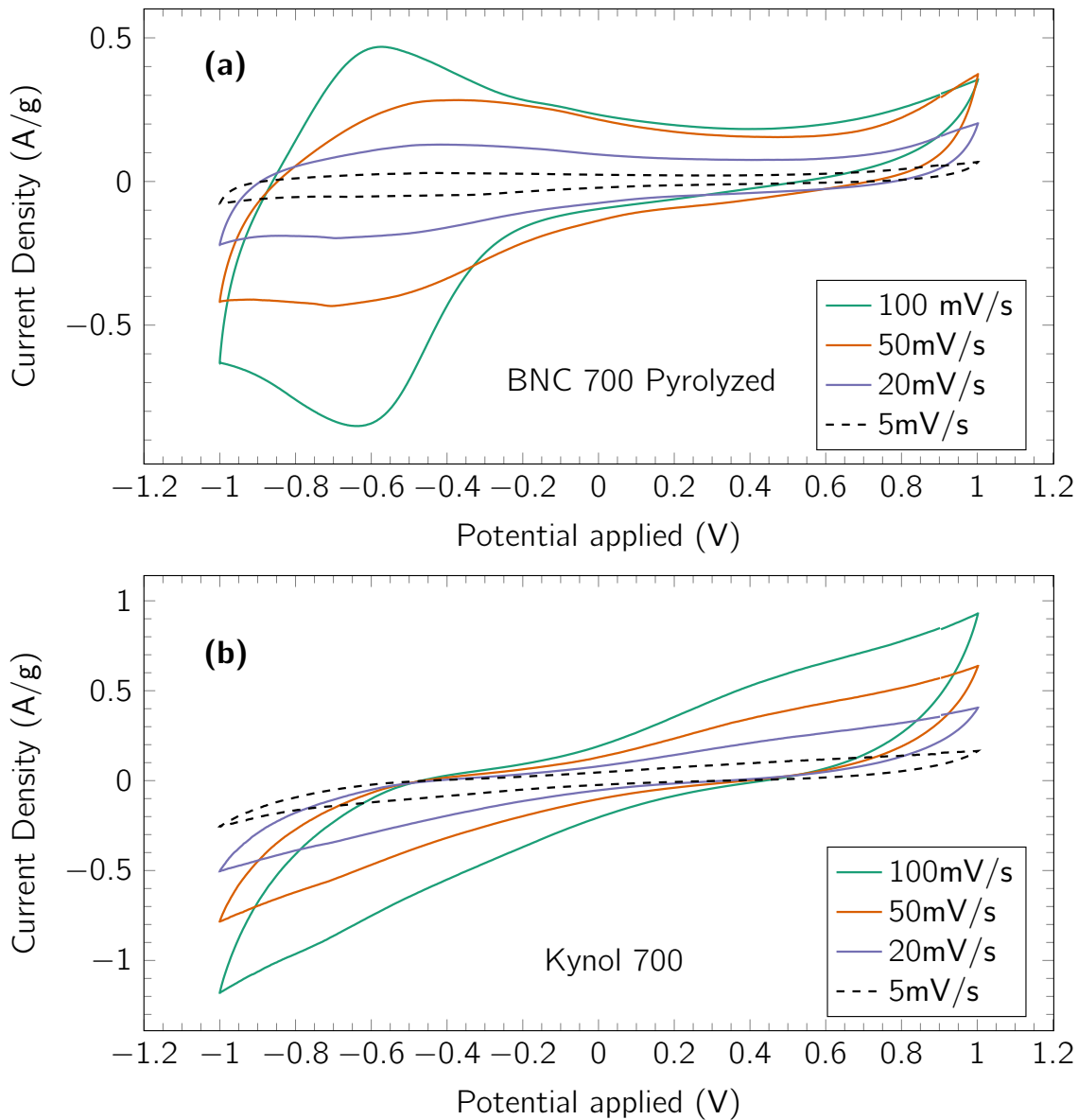
 Cyclic voltammetry. On (a), the BNC 700 Pyrolyzed sample with a more pseudocapacitance curve. On (b) Kynol 700 with symmetrical curve.
 Source: adapted, with permission, from Graciano B. De Souza et al. in Advances in Materials Science and Engineering ©① Hindawi (1).

In the Nyquist plot, shown in Figure 23, the Kynol sample shows a distorted semicircular shape at all tested frequencies. It also shows that the BNC sample has decreased both the real and imaginary impedance at higher frequency in an inductive loop. This change could be attributed to the diffusion difficulty at lower frequencies, which becomes

less important as the frequency increases. The inductive loop however maybe related to corrosion reactions at the electrode (118). Impedance is also represented in the Bode plot in Figure 23b, where all samples exhibited an almost ideal capacitor-like response.

Figure 23 – Nyquist plot and Bode plot
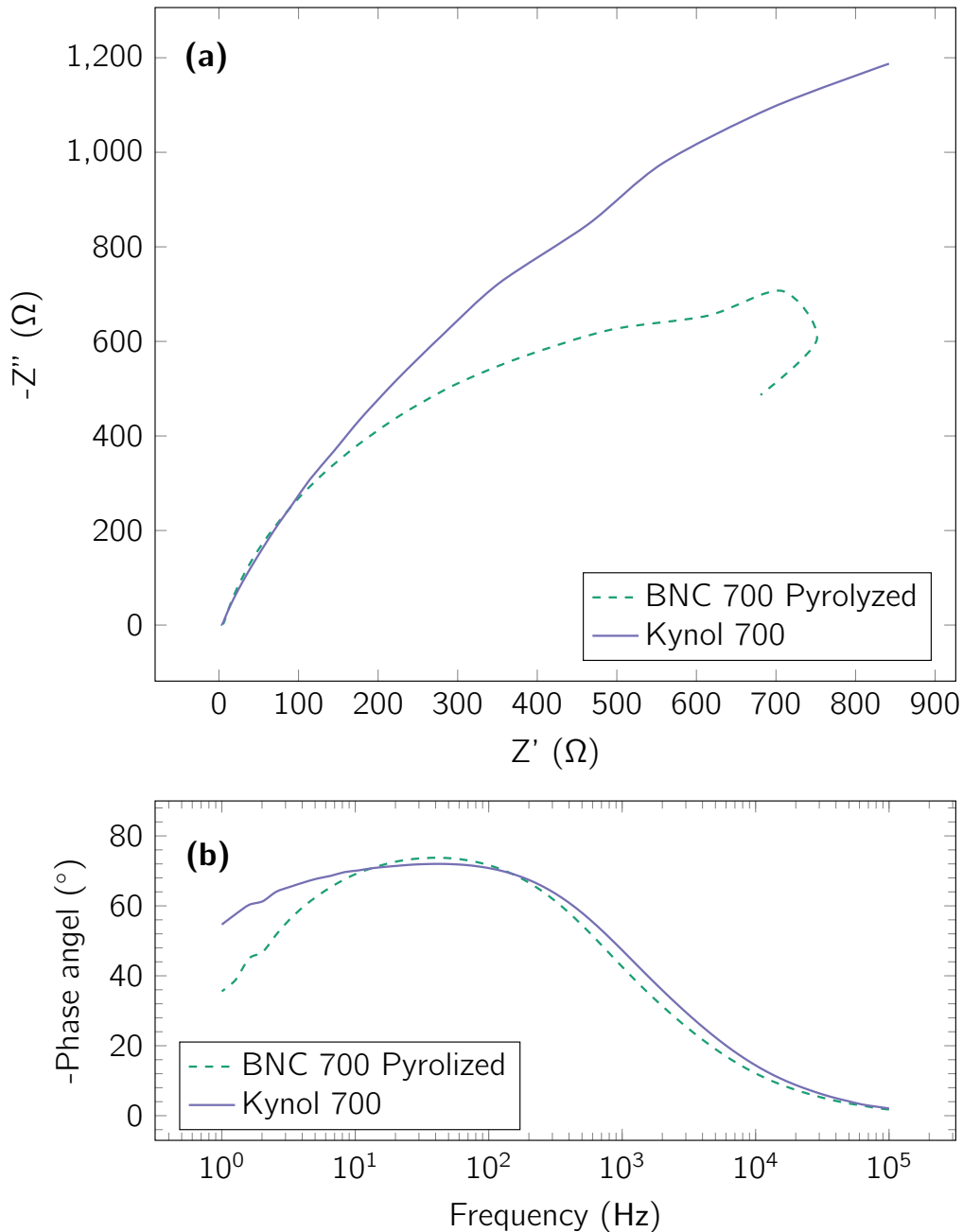
On (a) Nyquist plot and (b) Bode plot (100 kHz and 0.001 kHz)
Source: adapted, with permission, from Graciano B. De Souza et al. in Advances in Materials Science and Engineering ⓒ ⓘ Hindawi (1).

The galvanostatic charge-discharge is plotted in Figure 24. The Kynol sample displays an almost triangular profile of a supercapacitive charge storage. The pyrolyzed BNC

700 exhibited an asymmetrical profile, closer to a battery-like behavior, which is related to the layer thickness and textural structure.

Figure 24 – Galvanostatic charge-discharge over time
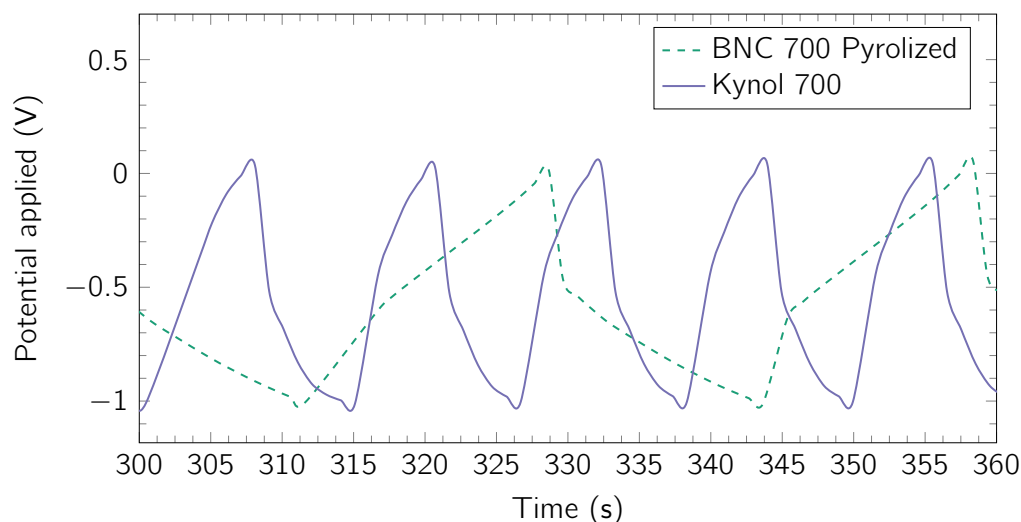
The specific capacitance, at $5\,\mathrm{mV\,s^{-1}}$, is displayed in Table 8. Figure 25 shows the relationship between the specific capacitance and the potential scanning rate, for both samples it decreases of the specific capacitance as the sweep rate increases. This could happen because with slower scan the electrolyte has more time to permeate deeper in between the fibers having a greater contact area with the surface of the electrode. This effect is more noticeable in the Kynol sample, probably due to the difference in macropore and fiber diameter (see Figure 17). This results are inline with other researches on carbon electrodes using KOH electrolyte (119).

Table 8 – Specific capacitance compared to the SSA

Sample	S_{BET} $(\mathrm{m^2\,g^{-1}})$	Specific Capacitance $(\mathrm{F\,g^{-1}})$
BNC 700 Pyrolyzed	175.65	5.61
Kynol 700	1 480.97	7.93

Figure 26 presents a Ragone plot, in specific capacitance, to compare the data with currently known devices. The values were calculated from the maximum discharge potential following the method used by Raut et al. (121). Both samples fit into the broad category of batteries with low energy density, which indicates that they are able to store a small

amount of energy but still capable of delivering this energy fast enough to be considered a battery. Overlooking the low energy density, we can see that the power density is similar to a porous nickel oxide/carbon electrode built by Wang et al. (122).

Figure 25 – Specific capacitance versus sweep rate.
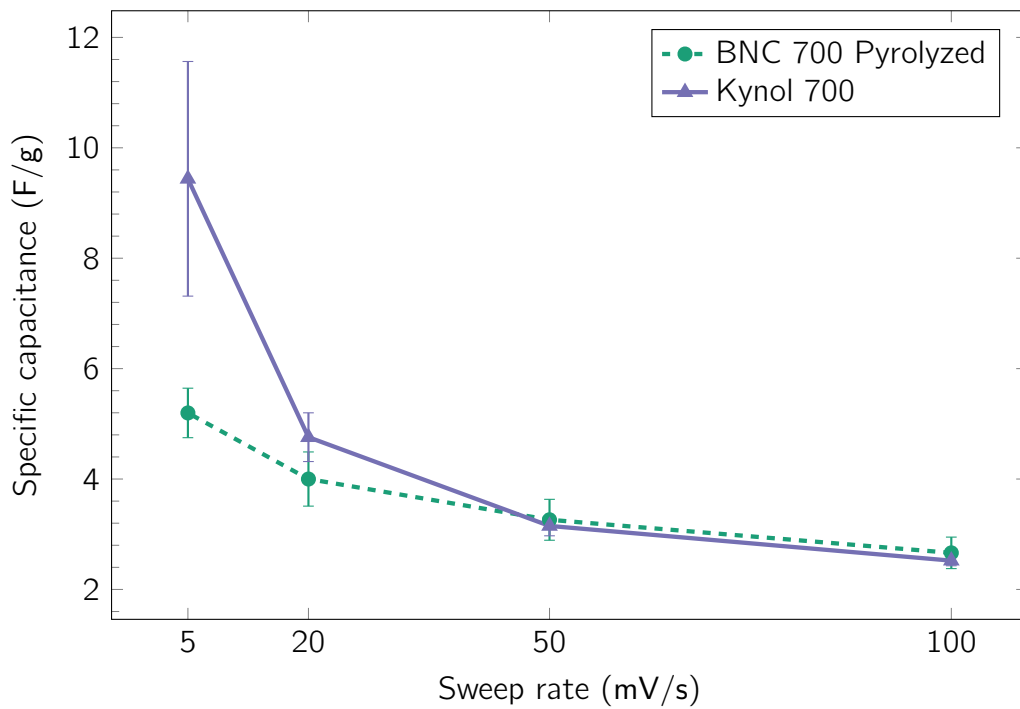
Figure 26 – Ragone plot relating energy density with power density.
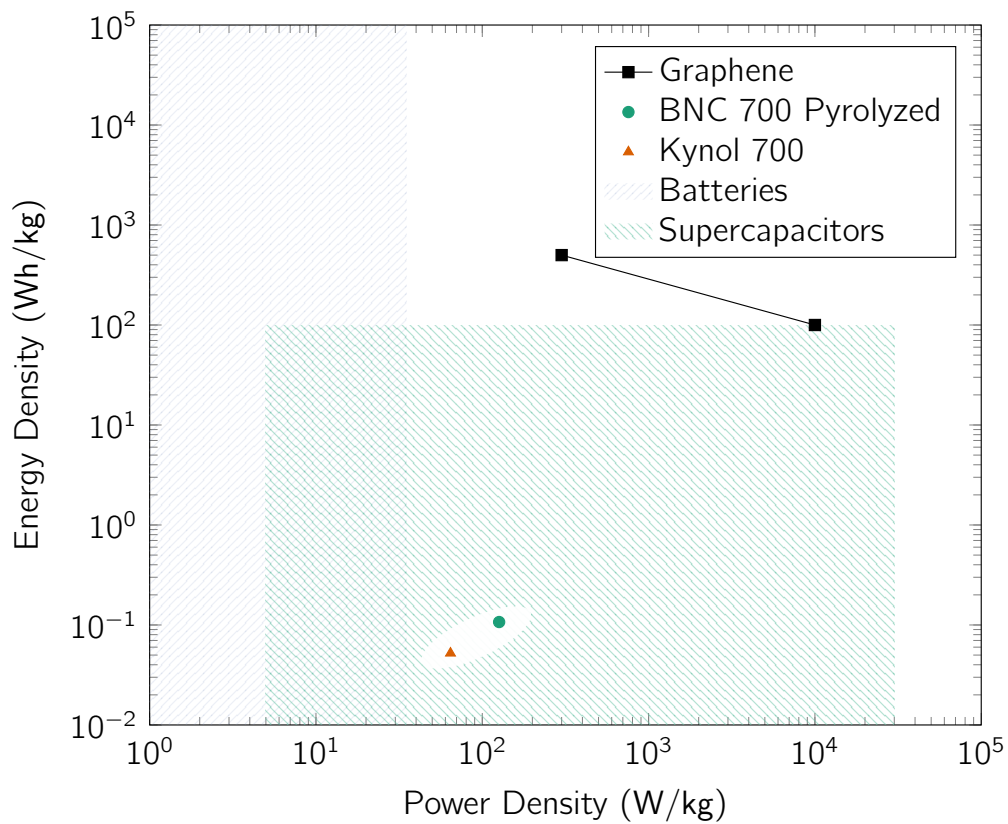
The hatched green area corresponds to the usual batteries limit and hatched purple to supercapacitors.
Added Graphene State of the Art for comparison, adapted from (120).
Source: adapted, with permission, from Graciano B. De Souza et al. in Advances in Materials Science and Engineering ⓒ⊕ Hindawi (1).

6 Conclusions

██

""Pride," said Imlac, "is seldom delicate; it will please itself with very mean advantages, and envy feels not its own happiness but when it may be compared with the misery of others."

Samuel Johnson, 1759, Rasselas, Prince of Abyssinia, Chapter 9.

In this work it was proven that a bulk (2 mm in height) highly porous material, more specifically bacterial nanocellulose and Kynol, both with fibers below 2 μm thick, can be successfully coated with TiO_2 via atomic layer deposition, as demonstrated by the SEM images (see Figure 17). In both samples the nanostructure retained its original arrangement of the fibers after the deposition cycles. As other have demonstrated before, but with different porous substrate, despite the tortuosity of their porosity. So it was found that BNC and non-woven felts can also be coated via ALD as long as the pores remain open and wide enough for the gaseous to flow. A decrease in the surface area, as expected, was also observed from the nitrogen adsortion.

Throught the XRD analysis it was found that the pyrolysis of the BNC coated sample, in a single heat-treatment step in inert atmosphere, yielded a compound of carbon and anatase phase. When deposited at 95 °C, titanium isopropoxide transformed into, and stayed in, the anatase phase even after heat treatment at 800 °C. This is above the usual phase transformation for titania, from anatase into rutile. Such fact have only been documented a few times before, when dealing with nano layers of titania. So the findings in this thesis adds to the literature of anatase stabilization phenomena in the nano-scale titania. Although the current theory for this phase stabilization is fairly new, and up to debate, the given explanation fits very well with the parameters and material thickness used in this work. The phase transformation seems to be require a nano-particle aggregations since the phase nucleation happens at particle-to-particle contacts. Due to the high porosity the contact between the layers of different fibers is fairly limited, which could match the proposed mechanism in the literature (43).

In addition, the TiO_2 layer maintains its shape and structure when the fibers were removed, through burning of the Kynol sample, generating titania tubes with nanometric wall thickness. These hollow fibers are expected to contain an even larger surface area. As single-component substrate they can see many other uses or even pass through an additional ALD process to form multi-material compounds.

Despite their relatively low capacitance, these properties could allow carbon fibrous coated with titania to be used in electrochemical energy storage devices once some settings get fine-tuned. Varying parameters such as:

- ALD thickness;

- Pyrolysis temperature;

- Electrolyte composition;

- Electrolyte concentration;

- Active material weight proportion on the electrode assembly;

could be very useful for future work.

REFERENCES

1 SOUZA, Graciano B. De et al. Functionalization of Carbon Electrodes with Nanotitania by Atomic Layer Deposition. Ed. by Marco Rossi. **Advances in Materials Science and Engineering**, Hindawi Limited, v. 2022, p. 1–12, Oct. 2022. DOI: 10.1155/2022/9575845.

2 RAMBO, C.R. et al. Manufacturing of biomorphic (Si, Ti, Zr)-carbide ceramics by sol–gel processing. **Carbon**, Elsevier BV, v. 43, n. 6, p. 1174–1183, 2005. DOI: 10.1016/j.carbon.2004.12.009.

3 IGUCHI, M.; YAMANAKA, S.; BUDHIONO, A. Bacterial cellulose — a masterpiece of nature's arts. **J. Mater. Sci.**, Springer Nature, v. 35, n. 2, p. 261–270, 2000. DOI: 10.1023/A:1004775229149.

4 LEE, Seung-Mo. **Atomic layer deposition on biological matter**: Übers. des Hauptsacht.: Atomlagenabscheidung auf biologische Materialien. 10 Jan. 2009. S. 145. PhD thesis – Albert-Ludwigs-Universität Freiburg, Breisgau, Germany. URN: urn:nbn:de:bsz:25-opus-71425.

5 VITIELLO, J.; PIALLAT, F.; BONNET, L. Alternative deposition solution for cost reduction of TSV integration. **International Symposium on Microelectronics**, IMAPS - International Microelectronics Assembly and Packaging Society, v. 2017, n. 1, p. 000135–000139, Oct. 2017. DOI: 10.4071/isom-2017-tp52_034.

6 WASA, Kiyotaka. **Handbook of Sputter Deposition Technology Fundamentals and Applications for Functional Thin Films, Nano-Materials and MEMS**: Fundamentals and Applications for Functional Thin Films, Nano-Materials and MEMS. Ed. by Kiyotaka Wasa, Isaku Kanno and Hidetoshi Kotera. Second Edition. [S.l.]: Elsevier Science & Technology Books, 2012. P. 660. 660 pp. ISBN 9781437734836.

7 LÜHN, O. et al. Barrier and seed layer coverage in 3D structures with different aspect ratios using sputtering and ALD processes. **Microelectronic Engineering**, Elsevier BV, v. 85, n. 10, p. 1947–1951, Oct. 2008. DOI: 10.1016/j.mee.2008.06.007.

8 JOHNSON, Richard W.; HULTQVIST, Adam; BENT, Stacey F. A brief review of atomic layer deposition: from fundamentals to applications. **Materials Today**, Elsevier BV, v. 17, n. 5, p. 236–246, June 2014. DOI: 10.1016/j.mattod.2014.04.026.

9 BEGUIN, Francois; FRACKOWIAK, Elzbieta; LU, Max. **Supercapacitors**: Materials, Systems, and Applications. Ed. by Edited by François Béguin and Elżbieta Frąckowiak. [S.l.]: Wiley-VCH, 16 Apr. 2013. P. 568. 528 pp. ISBN 9783527646692.

10 ALBERTIN, K.F.; PEREYRA, I. Study of reactive sputtering titanium oxide for metal-oxide-semiconductor capacitors. **Thin Solid Films**, Elsevier BV, v. 517, n. 16, p. 4548–4554, June 2009. DOI: 10.1016/j.tsf.2008.12.045.

11 MANTZILA, Aikaterini G.; PRODROMIDIS, Mamas I. Performance of Impedimetric Biosensors Based on Anodically Formed Ti/TiO2 Electrodes. **Electroanalysis**, Wiley, v. 17, n. 20, p. 1878–1885, Oct. 2005. DOI: 10.1002/elan.200503306.

12 REDDY, K Madhusudan; MANORAMA, Sunkara V; REDDY, A Ramachandra. Bandgap studies on anatase titanium dioxide nanoparticles. **Materials Chemistry and Physics**, Elsevier BV, v. 78, n. 1, p. 239–245, Feb. 2003. DOI: 10.1016/s0254-0584(02)00343-7.

13 YANG, Xiao Hua et al. Ultra-thin anatase TiO2 nanosheets dominated with {001} facets: thickness-controlled synthesis, growth mechanism and water-splitting properties. **CrystEngComm**, Royal Society of Chemistry (RSC), v. 13, n. 5, p. 1378–1383, 2011. DOI: 10.1039/c0ce00233j.

14 SANJINÉS, R. et al. Electronic structure of anatase TiO2 oxide. **Journal of Applied Physics**, AIP Publishing, v. 75, n. 6, p. 2945–2951, Mar. 1994. DOI: 10.1063/1.356190.

15 MALYGIN, Anatolii A. et al. From V. B. Aleskovskii's "Framework" Hypothesis to the Method of Molecular Layering/Atomic Layer Deposition. **Chem. Vap. Deposition**, Wiley, v. 21, n. 10-11-12, p. 216–240, 2015. DOI: 10.1002/cvde.201502013.

16 AHVENNIEMI, Esko et al. Review Article: Recommended reading list of early publications on atomic layer deposition—Outcome of the "Virtual Project on the History of ALD". **Journal of Vacuum Science & Technology A: Vacuum, Surfaces, and Films**, American Vacuum Society, v. 35, n. 1, p. 010801, Jan. 2017. DOI: 10.1116/1.4971389.

17 OY, PLANAR INTERNATIONAL A CORP OF FINLAND. Suntola Tuomo; Antson Jorma. **Method for producing compound thin films**. 25 Nov. 1975. US4058430A.

18 RITALA, Mikko; LESKELÄ, Markku. **Deposition ans Processing of Thin Films**: Atomic layer deposition. [S.l.]: Academic Press, Dec. 2002. P. 5. ISBN 0125129092. DOI: 10.1201/9781420034141.sec2.

19 ORWANT, Jon; BROCKMAN, Will. **Google Books Ngram Viewer**. Ed. by Google inc. 6 Oct. 2021. Available at:
`https://books.google.com/ngrams/graph?content=atomic+`
`layer+deposition%2Catomic+layer+epitaxy&year_start=`
`1940&year_end=2019&corpus=26&smoothing=0&direct_url=`
`t1%3B%2Catomic%20layer%20deposition%3B%2Cc0%3B.t1%3B%`
`2Catomic%20layer%20epitaxy%3B%2Cc0#`. Visited on: 30 Oct. 2021.

20 GEORGE, Steven M. Atomic Layer Deposition: An Overview. **Chem. Rev.**, American Chemical Society (ACS), v. 110, n. 1, p. 111–131, Jan. 2010. DOI: 10.1021/cr900056b.

21   RAHTU, A.; RITALA, M. Reaction Mechanism Studies on Titanium Isopropoxide–Water Atomic Layer Deposition Process. **Chemical Vapor Deposition**, Wiley, v. 8, n. 1, p. 21, Jan. 2002. DOI: 10.1002/1521-3862(20020116)8:1<21::aid-cvde21>3.0.co;2-0.

22   POODT, Paul et al. Spatial atomic layer deposition: A route towards further industrialization of atomic layer deposition. **Journal of Vacuum Science & Technology A: Vacuum, Surfaces, and Films**, American Vacuum Society, v. 30, n. 1, p. 010802, Jan. 2012. DOI: 10.1116/1.3670745.

23   GRANNEMAN, Ernst et al. Batch ALD: Characteristics, comparison with single wafer ALD, and examples. **Surf. Coat. Technol.**, Elsevier BV, v. 201, n. 22-23, p. 8899–8907, Sept. 2007. DOI: 10.1016/j.surfcoat.2007.05.009.

24   POWER PORTFOLIO, LLC ast. David L. Hagen et al. **Trifluid reactor**. 28 Apr. 2009. US7523603B2.

25   RAADT, BSP de. **Spatial ALD of zinc tin oxide**: Growth and characterization of zinc tin oxide thinfilms deposited by co-injection spatial atomic layerdeposition. 5 June 2015. S. 88. MA thesis – Eindhoven University of Technology. p. 14.

26   CREMERS, Véronique; PUURUNEN, Riikka L.; DENDOOVEN, Jolien. Conformality in atomic layer deposition: Current status overview of analysis and modelling. **Applied Physics Reviews**, AIP Publishing, v. 6, n. 2, p. 021302, June 2019. DOI: 10.1063/1.5060967.

27   YANGUAS-GIL, Angel. **Growth and Transport in Nanostructured Materials**. [S.l.]: Springer-Verlag GmbH, 30 Nov. 2016. ISBN 978-3-319-24672-7.

28   STICKING coefficient in surface chemistry. In: IUPAC Compendium of Chemical Terminology. 2. ed. [S.l.]: IUPAC. DOI: 10.1351/goldbook.S06012.

29   KNOOPS, H.C.M. et al. Atomic Layer Deposition. In: HANDBOOK of Crystal Growth. [S.l.]: Elsevier, 2015. P. 1101–1134. DOI: 10.1016/b978-0-444-63304-0.00027-5.

30   WORLD HEALTH ORGANIZATION. **AMMONIA (ANHYDROUS) ICSC: 0414**. International Chemical Safety Card. [S.l.], 16 Oct. 2013. Available at: `https://www.ilo.org/dyn/icsc/showcard.display?p_lang=en&p_card_id=0414&p_version=2`.

31   RAHTU, A.; RITALA, M. Reaction Mechanism Studies on Titanium Isopropoxide–Water Atomic Layer Deposition Process. **Chem. Vap. Deposition**, Wiley, v. 8, n. 1, p. 21, Jan. 2002. DOI: 10.1002/1521-3862(20020116)8:1<21::aid-cvde21>3.0.co;2-0.

32 SHEVJAKOV, AM; KUZNETSOVA, GN; ALESKOVSKII, VB. Interaction of titanium and germanium tetrachlorides with hydroxylated silicon dioxide. In: CHEMISTRY of High Temperature Materials. Proceedings of the 2nd USSR Conference on High Temperature Chemistry of Oxides. [S.l.: s.n.]. P. 149–155.

33 ALURU, Narayan; BESKOK, Ali; KARNIADAKIS, George. **Microflows and Nanoflows**. [S.l.]: Springer New York, 5 July 2005. 840 pp. ISBN 0387221972.

34 KIM, Hyungjun. Atomic layer deposition of metal and nitride thin films: Current research efforts and applications for semiconductor device processing. **Journal of Vacuum Science & Technology B:** Microelectronics and Nanometer Structures Processing, Measurement, and Phenomena, American Vacuum Society, v. 21, n. 6, p. 2231, 2003. IBM Research Division. DOI: 10.1116/1.1622676.

35 MUÑOZ-ROJAS, D. et al. Speeding up the unique assets of atomic layer deposition. **Materials Today Chemistry**, Elsevier BV, v. 12, p. 96–120, June 2019. DOI: 10.1016/j.mtchem.2018.11.013.

36 AFIF, Abdulla Bin et al. Atomic layer deposition of perovskites - Part 1: Fundamentals of nucleation and growth. **Material Design & Processing Communications**, Hindawi Limited, v. 2, n. 1, Dec. 2019. DOI: 10.1002/mdp2.114.

37 MADADI, Milad et al. Atomic and Molecular Layer Deposition of Alkali Metal Based Thin Films. **ACS Applied Materials & Interfaces**, American Chemical Society (ACS), v. 13, n. 48, p. 56793–56811, Nov. 2021. DOI: 10.1021/acsami.1c17519.

38 ELAM, Jeffrey W. et al. Atomic Layer Deposition for the Conformal Coating of Nanoporous Materials. **J Nanomater**, Hindawi Limited, v. 2006, p. 1–5, 2006. DOI: 10.1155/jnm/2006/64501.

39 TOMPKINS, Harland; IRENE, Eugene A. **Handbook of Ellipsometry (Materials Science and Process Technology)**. [S.l.]: William Andrew, 2006. ISBN 9780815514992.

40 NGO, Dien et al. Spectroscopic ellipsometry study of thickness and porosity of the alteration layer formed on international simple glass surface in aqueous corrosion conditions. **npj Materials Degradation**, Springer Science and Business Media LLC, v. 2, n. 1, July 2018. DOI: 10.1038/s41529-018-0040-7.

41 FURLAN, Kaline P. et al. Highly porous α-Al2O3 ceramics obtained by sintering atomic layer deposited inverse opals. **Ceram. Int.**, Elsevier BV, v. 43, n. 14, p. 11260–11264, Oct. 2017. DOI: 10.1016/j.ceramint.2017.05.176.

42 ZHU, Shengyun; LIU, Junqing; SUN, Jiaming. Growth of ultrathin SnO2 on carbon nanotubes by atomic layer deposition and their application in lithium ion battery anodes. **Appl. Surf. Sci.**, Elsevier BV, v. 484, p. 600–609, Aug. 2019. DOI: 10.1016/j.apsusc.2019.04.163.

43 PASQUARELLI, Robert M. et al. Enhanced structural and phase stability of titania inverse opals. **J. Eur. Ceram. Soc.**, Elsevier BV, v. 35, n. 11, p. 3103–3109, Oct. 2015. DOI: 10.1016/j.jeurceramsoc.2015.04.041.

44 GAKIS, Georgios P. et al. Investigation of the initial deposition steps and the interfacial layer of Atomic Layer Deposited (ALD) Al2O3 on Si. **Applied Surface Science**, Elsevier BV, v. 492, p. 245–254, Oct. 2019. DOI: 10.1016/j.apsusc.2019.06.215.

45 CAO, Yan-Qiang et al. Atomic layer deposition of ZnO/TiO2 nanolaminates as ultra-long life anode material for lithium-ion batteries. **Sci. Rep.**, Springer Science and Business Media LLC, v. 9, n. 1, Aug. 2019. DOI: 10.1038/s41598-019-48088-2.

46 CAO, Yan-Qiang et al. Enhanced visible light photocatalytic activity of Fe2O3 modified TiO2 prepared by atomic layer deposition. **Sci. Rep.**, Springer Science and Business Media LLC, v. 10, n. 1, Aug. 2020. DOI: 10.1038/s41598-020-70352-z.

47 TROUGHT, Mikhail et al. Influence of surface etching and oxidation on the morphological growth of Al2O3 by ALD. **Surf. Sci.**, Elsevier BV, v. 690, p. 121479, Dec. 2019. DOI: 10.1016/j.susc.2019.121479.

48 AN, Seongpil et al. Supersonic Cold Spraying for Energy and Environmental Applications: One-Step Scalable Coating Technology for Advanced Micro- and Nanotextured Materials. **Advanced Materials**, Wiley, v. 32, n. 2, p. 1905028, Nov. 2019. DOI: 10.1002/adma.201905028.

49 DARWISH, Ghaith et al. Improving Polymethyl Methacrylate Resin Using a Novel Titanium Dioxide Coating. **Journal of Prosthodontics**, Wiley, v. 28, n. 9, p. 1011–1017, Feb. 2019. DOI: 10.1111/jopr.13032.

50 BUI, H. Van; GRILLO, F.; OMMEN, J. R. van. Atomic and molecular layer deposition: off the beaten track. **Chemical Communications**, Royal Society of Chemistry (RSC), v. 53, n. 1, p. 45–71, 2017. DOI: 10.1039/c6cc05568k.

51 NORRRAHIM, Mohd Nor Faiz et al. Nanocellulose: the next super versatile material for the military. **Materials Advances**, Royal Society of Chemistry (RSC), v. 2, n. 5, p. 1485–1506, 2021. DOI: 10.1039/d0ma01011a.

52 JOSEPH S. HAYES, Jr. Nanostructure of Activated Carbon Fibers and Kinetics of Adsorption/Desorption. In: AIR & Waste Management Association, 95th Annual Conference and Exhibition. Baltimore, MD, United States: [s.n.], 23 July 2002. v. 43052, p. 689–710.

53 ELLEBRACHT, Nathan C.; JONES, Christopher W. Amine functionalization of cellulose nanocrystals for acid–base organocatalysis: surface chemistry, cross-linking, and solvent effects. **Cellulose**, Springer Science and Business Media LLC, v. 25, n. 11, p. 6495–6512, Sept. 2018. DOI: 10.1007/s10570-018-2043-5.

54 HABIBI, Youssef. Key advances in the chemical modification of nanocelluloses. **Chem. Soc. Rev.**, Royal Society of Chemistry (RSC), v. 43, n. 5, p. 1519–1542, 2014. DOI: 10.1039/c3cs60204d.

55 LIU, Hongzhi et al. Review on the Aerogel-Type Oil Sorbents Derived from Nanocellulose. **ACS Sustainable Chemistry - Engineering**, American Chemical Society (ACS), v. 5, n. 1, p. 49–66, Dec. 2016. DOI: 10.1021/acssuschemeng.6b02301.

56 REVIN, Viktor V. et al. Characterizing Bacterial Cellulose Produced byKomagataeibacter sucrofermentans H-110 on Molasses Medium and Obtaining a Biocomposite Based on It for the Adsorption of Fluoride. **Polymers**, MDPI AG, v. 13, n. 9, p. 1422, Apr. 2021. DOI: 10.3390/polym13091422.

57 SIMON, Patrice; GOGOTSI, Yury. Materials for electrochemical capacitors. **Nature Materials**, Nature Publishing Group, v. 7, n. 11, p. 845–854, Nov. 2008. DOI: 10.1038/nmat2297.

58 JIANG, Yong et al. Atomic layer deposition for improved lithiophilicity and solid electrolyte interface stability during lithium plating. **Energy Storage Materials**, Elsevier BV, v. 28, p. 17–26, June 2020. DOI: 10.1016/j.ensm.2020.01.019.

59 KORHONEN, Juuso T. et al. Inorganic Hollow Nanotube Aerogels by Atomic Layer Deposition onto Native Nanocellulose Templates. **ACS Nano**, American Chemical Society (ACS), v. 5, n. 3, p. 1967–1974, Mar. 2011. DOI: 10.1021/nn200108s.

60 MA, Lina et al. Flexible and Freestanding Supercapacitor Electrodes Based on Nitrogen-Doped Carbon Networks/Graphene/Bacterial Cellulose with Ultrahigh Areal Capacitance. **ACS Appl. Mater. Interface**, American Chemical Society (ACS), v. 8, n. 49, p. 33608–33618, Dec. 2016. DOI: 10.1021/acsami.6b11034.

61 LI, Yi et al. Thermally Stimulated Wettability Transformations on One-Cycle Atomic Layer Deposition-Coated Cellulosic Paper: Applications for Droplet Manipulation and Heat Patterned Paper Fluidics. **ACS Applied Materials & Interfaces**, American Chemical Society (ACS), v. 13, n. 11, p. 13802–13812, Mar. 2021. DOI: 10.1021/acsami.0c22672.

62 AKYILDIZ, Halil I.; DILER, Sumeyye; ISLAM, Shafiqul. Evaluation of TiO2 and ZnO atomic layer deposition coated polyamide 66 fabrics for photocatalytic activity and antibacterial applications. **Journal of Vacuum Science & Technology A**, American Vacuum Society, v. 39, n. 2, p. 022405, Mar. 2021. DOI: 10.1116/6.0000761.

63 KLEMM, Dieter et al. Cellulose: Fascinating Biopolymer and Sustainable Raw Material. **Angew. Chem. - Int. Ed.**, Wiley, v. 44, n. 22, p. 3358–3393, 2005. DOI: 10.1002/anie.200460587.

64   PARKES, Alexander. Alexander Parkes. **Chronological and descriptive index of patents applied for and patents granted, containing the abridgements of provisional and complete specifications.** Printed and published by order of the Commissioner of Patents, 15 & 16 Victoriae, Cap. 83. Sec. XXXII. Britain., Great, 11 May 1865. n. 1313.

65   BROWN, Adrian J. XLIII.—On an acetic ferment which forms cellulose. **J. Chem. Soc., Trans.**, Royal Society of Chemistry (RSC), v. 49, n. 0, p. 432–439, 0 1886. DOI: 10.1039/ct8864900432.

66   HESTRIN, S.; ASCHNER, M.; MAGER, J. Synthesis of Cellulose by Resting Cells of Acetobacter xylinum. **Nature**, Springer Nature, v. 159, n. 4028, p. 64–65, 1947. DOI: 10.1038/159064a0.

67   QIU, Kaiyan; NETRAVALI, Anil N. A Review of Fabrication and Applications of Bacterial Cellulose Based Nanocomposites. **Polym Rev**, Informa UK Limited, v. 54, n. 4, p. 598–626, 2014. DOI: 10.1080/15583724.2014.896018.

68   SHAH, Nasrullah et al. Overview of bacterial cellulose composites: A multipurpose advanced material. **Carbohydr. Polym.**, Elsevier BV, v. 98, n. 2, p. 1585–1598, 2013. DOI: 10.1016/j.carbpol.2013.08.018.

69   BRANDES, Ricardo et al. A Mini-Review on the Progress of Spherical Bacterial Cellulose Production. **J Nano Res**, Trans Tech Publications, v. 45, p. 142–154, 2017. DOI: 10.4028/www.scientific.net/jnanor.45.142.

70   GORGIEVA; TRČEK. Bacterial Cellulose: Production, Modification and Perspectives in Biomedical Applications. **Nanomaterials**, MDPI AG, v. 9, n. 10, p. 1352, 2019. DOI: 10.3390/nano9101352.

71   YOSHINAGA, Fumihiro; TONOUCHI, Naoto; WATANABE, Kunihiko. Research Progress in Production of Bacterial Cellulose by Aeration and Agitation Culture and Its Application as a New Industrial Material. **Biosci. Biotechnol. Biochem.**, Informa UK Limited, v. 61, n. 2, p. 219–224, 1997. DOI: 10.1271/bbb.61.219.

72   PARTE, Francisco German Blanco et al. Current progress on the production, modification, and applications of bacterial cellulose. **Crit. Rev. Biotechnol.**, Informa UK Limited, v. 40, n. 3, p. 397–414, Jan. 2020. DOI: 10.1080/07388551.2020.1713721.

73   RÜHS, Patrick A. et al. 3D bacterial cellulose biofilms formed by foam templating. **npj Biofilms Microbiomes**, Springer Nature America, Inc, v. 4, n. 1, Sept. 2018. DOI: 10.1038/s41522-018-0064-3.

74   SWINGLER, Sam et al. Recent Advances and Applications of Bacterial Cellulose in Biomedicine. **Polymers**, MDPI AG, v. 13, n. 3, p. 412, Jan. 2021. DOI: 10.3390/polym13030412.

75 CAVALCANTI, Luciana Marins et al. Efficacy of bacterial cellulose membrane for the treatment of lower limbs chronic varicose ulcers: a randomized and controlled trial. **Revista do Colégio Brasileiro de Cirurgiões**, FapUNIFESP (SciELO), v. 44, n. 1, p. 72–80, Feb. 2017. DOI: 10.1590/0100-69912017001011.

76 KIM, Jangho et al. Bacterial Cellulose Nanofibrillar Patch as a Wound Healing Platform of Tympanic Membrane Perforation. **Adv. Healthcare Mater.**, Wiley, v. 2, n. 11, p. 1525–1531, Apr. 2013. DOI: 10.1002/adhm.201200368.

77 GAO, Minghong et al. A natural in situ fabrication method of functional bacterial cellulose using a microorganism. **Nat Commun**, Springer Science and Business Media LLC, v. 10, n. 1, 25 Jan. 2019. DOI: 10.1038/s41467-018-07879-3.

78 BÉGUIN, François et al. Carbons and Electrolytes for Advanced Supercapacitors. **Advanced Materials**, Wiley, v. 26, n. 14, p. 2219–2251, Feb. 2014. DOI: 10.1002/adma.201304137.

79 PALAGONIA, Maria Sofia et al. Comparison between cyclic voltammetry and differential charge plots from galvanostatic cycling. **J. Electroanal. Chem.**, Elsevier BV, v. 847, p. 113170, Aug. 2019. DOI: 10.1016/j.jelechem.2019.05.052.

80 COMMONS, Wikimedia. **File:Cyclic voltammetry, the case of one-electron transfer to a free-diffusing molecule.svg — Wikimedia Commons, the free media repository**. Ed. by the free media repository Wikimedia Commons. [S.l.: s.n.], 28 Oct. 2020. [Online; accessed 10-October-2022]. Available at: `https://commons.wikimedia.org/w/index.php?title=File: Cyclic_voltammetry,_the_case_of_one- electron_transfer_to_a_free- diffusing_molecule.svg&oldid=504802137`. Lewisiscrazy.

81 ZHANG, Li Li; ZHAO, X. S. Carbon-based materials as supercapacitor electrodes. **Chem. Soc. Rev.**, Royal Society of Chemistry (RSC), v. 38, n. 9, p. 2520, 2009. DOI: 10.1039/b813846j.

82 POONAM et al. Review of supercapacitors: Materials and devices. **Journal of Energy Storage**, Elsevier BV, v. 21, p. 801–825, Feb. 2019. DOI: 10.1016/j.est.2019.01.010.

83 CALLEGARO, Luca. **Electrical Impedance Principles, Measurement, and Applications**: Principles, Measurement, and Applications. [S.l.]: Taylor & Francis Group, 2012. P. 308. ISBN 9780429065576.

84 THE EDITORS OF ENCYCLOPAEDIA BRITANNICA. electrical impedance: Matter & Energy. In: **Science**: Physics. [S.l.: s.n.], 29 Sept. 2022.

85   CESCA, Karina et al. Synthesis of spherical bacterial nanocellulose as a potential silver adsorption agent for antimicrobial purposes. **Cellulose Chemistry And Technology**, EDITURA ACAD ROMANE CALEA 13 SEPTEMBRIE NR 13, SECTOR 5, BUCURESTI 050711, v. 54, n. 3-4, p. 285–290, 1 Nov. 2019.

86   ALTOMARE, Angela et al. QUALX2.0: a qualitative phase analysis software using the freely available database POW_COD. **J. Appl. Crystallogr.**, International Union of Crystallography (IUCr), v. 48, n. 2, p. 598–603, Feb. 2015. DOI: 10.1107/S1600576715002319.

87   DOEBELIN, Nicola; KLEEBERG, Reinhard. Profex: a graphical user interface for the Rietveld refinement programBGMN. **J. Appl. Crystallogr.**, International Union of Crystallography (IUCr), v. 48, n. 5, p. 1573–1580, Aug. 2015. DOI: 10.1107/S1600576715014685.

88   LOWELL, S. et al. **Characterization of Porous Solids and Powders: Surface Area, Pore Size and Density**. [S.l.]: Springer Netherlands, 2004. DOI: 10.1007/978-1-4020-2303-3.

89   SKOPIN, E.V. et al. In situ ellipsometry monitoring of TiO2 atomic layerdeposition from Tetrakis(dimethylamido)titanium(IV)and H2O precursors on Si and In 0.53 Ga 0.47 Assubstrates. **Thin Solid Films**, Elsevier BV, v. 723, n. 8, p. 138591, Apr. 2021. DOI: 10.1016/j.tsf.2021.138591.

90   CHEN, Chuchu et al. Highly conductive nanocomposites based on cellulose nanofiber networks via NaOH treatments. **Composites Science and Technology**, Elsevier BV, v. 156, p. 103–108, Mar. 2018. DOI: 10.1016/j.compscitech.2017.12.029.

91   LEE, Wonsuk. **Overcoming parasitic reactions occurring in carbonaceous Seawater Battery cathodes and their mechanisms**. 10 Feb. 2021. S. 73. PhD thesis – Ulsan National Institute of Science and Technology, South Korea. CC BY-NC-ND 2.0 KR. Available at: `https://scholarworks.unist.ac.kr/handle/201301/50439`. Visited on: 1 Dec. 2021.

92   WALECZEK, Martin et al. Influence of Alumina Addition on the Optical Properties and the Thermal Stability of Titania Thin Films and Inverse Opals Produced by Atomic Layer Deposition. **Nanomaterials**, MDPI AG, v. 11, n. 4, p. 1053, Apr. 2021. DOI: 10.3390/nano11041053.

93   CASTIGLIONI, C. et al. Origin of the D line in the Raman spectrum of graphite: A study based on Raman frequencies and intensities of polycyclic aromatic hydrocarbon molecules. **J. Chem. Phys.**, AIP Publishing, v. 114, n. 2, p. 963, 2001. DOI: 10.1063/1.1329670.

94   COSTA, S et al. Characterization of carbon nanotubes by Raman spectroscopy. **Mater. Sci.-Pol.**, v. 26, n. 2, p. 433–441, 2008. ISSN 2083-134X.

95   FERRARI, A. C.; ROBERTSON, J. Interpretation of Raman spectra of disordered and amorphous carbon. **Physical Review B**, American Physical Society (APS), v. 61, n. 20, p. 14095–14107, May 2000. DOI: 10.1103/physrevb.61.14095.

96   SALAHUDDIN, Mohammad et al. Superhydrophobic PAN nanofibers for gas diffusion layers of proton exchange membrane fuel cells for cathodic water management. **Int. J. Hydrog. Energy**, Elsevier BV, v. 43, n. 25, p. 11530–11538, June 2018. DOI: 10.1016/j.ijhydene.2017.07.229.

97   LIU, Bingjun et al. Improving the performance of negative electrode for vanadium redox flow battery by decorating bismuth hydrogen edetate complex on carbon felt. **Ionics**, Springer Science and Business Media LLC, v. 25, n. 9, p. 4231–4241, May 2019. DOI: 10.1007/s11581-019-02988-5.

98   RAHMAWATI, Fitria; PUTRI, Fatmawati R.; MASYKUR, Abu. The Photocatalytic Activity of Zns-TiO2 on a Carbon Fiber Prepared by Chemical Bath Deposition. **Open Chemistry**, Walter de Gruyter GmbH, v. 17, n. 1, p. 132–141, Apr. 2019. DOI: 10.1515/chem-2019-0011.

99   TSOUKO, Erminda et al. Bacterial Cellulose Production from Industrial Waste and by-Product Streams. **Int J Mol Sci**, MDPI AG, v. 16, n. 12, p. 14832–14849, July 2015. DOI: 10.3390/ijms160714832.

100   ZHU, Pinwen et al. Titanium Carbide–Carbon Composite Nanofibers Prepared by Electrospinning Polyacrylonitrile. **Chemistry Letters**, The Chemical Society of Japan, v. 38, n. 8, p. 784–785, Aug. 2009. DOI: 10.1246/cl.2009.784.

101   KHALIL, Khalil et al. Titanium Carbide Nanofibers-Reinforced Aluminum Compacts, a New Strategy to Enhance Mechanical Properties. **Materials**, MDPI AG, v. 9, n. 5, p. 399, May 2016. DOI: 10.3390/ma9050399.

102   XIE, Zhen et al. Preparation of nano-sized titanium carbide particles via a vacuum carbothermal reduction approach coupled with purification under hydrogen/argon mixed gas. **RSC Advances**, Royal Society of Chemistry (RSC), v. 7, n. 15, p. 9037–9044, 2017. DOI: 10.1039/c6ra28264d.

103   LIANG, Jiajin et al. Comprehensive insights into cellulose structure evolution via multi-perspective analysis during a slow pyrolysis process. **Sustainable Energy & Fuels**, Royal Society of Chemistry (RSC), v. 2, n. 8, p. 1855–1862, 2018. DOI: 10.1039/c8se00166a.

104   O'BRIEN, S et al. Atomic Layer Deposition on Fabrics for Flame Resistance. **ECS Transactions**, The Electrochemical Society, v. 66, n. 40, p. 31–35, July 2015. DOI: 10.1149/06640.0031ecst.

105　OMERZU, Ales et al. Prevention of spontaneous combustion of cellulose with a thin protective Al 2 O 3 coating formed by atomic layer deposition. **Surface and Coatings Technology**, Elsevier BV, v. 333, p. 81–86, Jan. 2018. DOI: 10.1016/j.surfcoat.2017.10.067.

106　LI, Shiqi et al. Bacterial cellulose derived carbon nanofiber aerogel with lithium polysulfide catholyte for lithium–sulfur batteries. **Carbon**, Elsevier BV, v. 124, p. 212–218, Nov. 2017. DOI: 10.1016/j.carbon.2017.08.062.

107　TOBY, Brian H. R factors in Rietveld analysis: How good is good enough? **Powder Diffraction**, Cambridge University Press (CUP), v. 21, n. 1, p. 67–70, Mar. 2006. DOI: 10.1154/1.2179804.

108　SCARAMUZZO, Francesca A. et al. Phase Transition of TiO2 Nanotubes: a X-ray Study as a Function of Temperature. **The Journal of Physical Chemistry C**, American Chemical Society (ACS), v. 121, n. 44, p. 24871–24876, Oct. 2017. DOI: 10.1021/acs.jpcc.7b08297.

109　HANAOR, Dorian A. H.; SORRELL, Charles C. Review of the anatase to rutile phase transformation. **Journal of Materials Science**, Springer Science and Business Media LLC, v. 46, n. 4, p. 855–874, Dec. 2010. DOI: 10.1007/s10853-010-5113-0.

110　LEE, Jaesang et al. Deposition temperature dependence of titanium oxide thin films grown by remote-plasma atomic layer deposition. **physica status solidi (a)**, Wiley, v. 210, n. 2, p. 276–284, Oct. 2012. DOI: 10.1002/pssa.201228671.

111　HENEGAR, Alex J.; GOUGOUSI, Theodosia. Stability and Surface Reactivity of Anatase TiO2 Films. **ECS Journal of Solid State Science and Technology**, The Electrochemical Society, v. 4, n. 8, p298–p304, 2015. DOI: 10.1149/2.0041508jss.

112　GREGORY, Daniel G. et al. Template-Induced Structuring and Tunable Polymorphism of Three-Dimensionally Ordered Mesoporous (3DOm) Metal Oxides. **Langmuir**, American Chemical Society (ACS), v. 33, n. 26, p. 6601–6610, June 2017. DOI: 10.1021/acs.langmuir.7b01112.

113　ROSSI, L. et al. Thermal coarsening of individual titanate nanowires and their assemblies: Surface vs. bulk diffusion. **Ceramics International**, Elsevier BV, v. 46, n. 10, p. 16321–16327, July 2020. DOI: 10.1016/j.ceramint.2020.03.189.

114　DUAN, Chen-Long et al. Surface passivation of Fe3O4 nanoparticles with Al2O3 via atomic layer deposition in a rotating fluidized bed reactor. **Journal of Vacuum Science & Technology A: Vacuum, Surfaces, and Films**, American Vacuum Society, v. 34, n. 4, p. 04c103, July 2016. DOI: 10.1116/1.4952401.

115 LIEBNER, Falk et al. Aerogels from Unaltered Bacterial Cellulose: Application of scCO2 Drying for the Preparation of Shaped, Ultra-Lightweight Cellulosic Aerogels. **Macromol. Biosci.**, Wiley, v. 10, n. 4, p. 349–352, Feb. 2010. DOI: 10.1002/mabi.200900371.

116 NTAKIRUTIMANA, Samuel; TAN, Wei. Electrochemical capacitive behaviors of carbon/titania composite prepared by Tween 80-assisted sol-gel process for capacitive deionization. **Desalination**, Elsevier BV, v. 512, p. 115131, Sept. 2021. DOI: 10.1016/j.desal.2021.115131.

117 LIU, Hsin-Yu; WANG, Kai-Ping; TENG, Hsisheng. A simplified preparation of mesoporous carbon and the examination of the carbon accessibility for electric double layer formation. **Carbon**, Elsevier BV, v. 43, n. 3, p. 559–566, 2005. DOI: 10.1016/j.carbon.2004.10.020.

118 PHAM, Kien-Cuong et al. Graphene-Carbon Nanotube Hybrids as Robust Catalyst Supports in Proton Exchange Membrane Fuel Cells. **Journal of The Electrochemical Society**, The Electrochemical Society, v. 163, n. 3, f255–f263, 2016. DOI: 10.1149/2.0891603jes.

119 PAGKETANANG, Thanchanok et al. Microporous Activated Carbon from KOH-Activation of Rubber Seed-Shells for Application in Capacitor Electrode. **Energy Procedia**, Elsevier BV, v. 79, p. 651–656, Nov. 2015. DOI: 10.1016/j.egypro.2015.11.550.

120 VIVANCO, Juan Prieto; RODRIGUEZ-MONROY, Carlos. Graphene Applications in the Energy Field: State-of- the-Art and Impact. In: PROCEEDINGS of the 16th LACCEI International Multi-Conference for Engineering, Education, and Technology: "Innovation in Education and Inclusion". [S.l.]: Latin American and Caribbean Consortium of Engineering Institutions, 2018. DOI: 10.18687/laccei2018.1.1.444.

121 RAUT, Akshay S.; PARKER, Charles B.; GLASS, Jeffrey T. A method to obtain a Ragone plot for evaluation of carbon nanotube supercapacitor electrodes. **J. Mater. Res.**, Springer Science and Business Media LLC, v. 25, n. 8, p. 1500–1506, Aug. 2010. DOI: 10.1557/jmr.2010.0192.

122 WANG, Da-Wei; LI, Feng; CHENG, Hui-Ming. Hierarchical porous nickel oxide and carbon as electrode materials for asymmetric supercapacitor. **J. Power Sources**, Elsevier BV, v. 185, n. 2, p. 1563–1568, Dec. 2008. DOI: 10.1016/j.jpowsour.2008.08.032.